

# Exponential Accuracy Solutions of 2-D Electromagnetic Scattering From Multilayered Nonconcentric Elliptical Magnetodielectric Cylinders Under TE Illumination

Zhen Guan<sup>iD</sup>, Jiawen Li<sup>iD</sup>, and Feng Han<sup>iD</sup>, *Senior Member, IEEE*

**Abstract**—In this article, we develop the fast computation algorithm for electromagnetic (EM) scattering from 2-D multilayered nonconcentric elliptical magnetodielectric cylinders illuminated by an EM wave with transverse electric (TE) polarization. The dielectric materials filling each homogeneous cylinder can be isotropic or biaxially anisotropic. Meanwhile, each elliptical cylinder is allowed to have its own axis ratio. The multilayer surface integral equations (SIEs) are first formed and then transformed into the spectral-domain expressions by expanding both the unknown boundary tangential field values and Green’s functions with the Fourier series. The purpose of such a spectral integral method (SIM) is to lower the spatial sampling density (SD) along the multiple cylindrical boundaries and simultaneously maintain an exponentially decaying numerical error. Finally, the discretized matrix equations for SIM are assembled by letting the order of the Fourier series be equal to the number of total discretized points in each cylindrical boundary. Two numerical examples are presented to validate the computation accuracy and efficiency of the SIM when the material is either isotropic or biaxially anisotropic. It is found that the SIM has superiority over the traditional method of moments (MoM) for both the less computational time and exponentially decaying errors.

**Index Terms**—Anisotropic medium, multilayered magnetodielectric elliptical cylinders, spectral integral method (SIM), surface integral equations (SIEs).

## I. INTRODUCTION

ELectromagnetic (EM) scattering refers to the fundamental process that occurs when waves in a continuous medium interact with objects, which have obviously different dielectric properties [1]. This process will change the wave

Manuscript received 17 August 2023; revised 25 September 2023; accepted 26 September 2023. Date of publication 11 October 2023; date of current version 7 May 2024. This work was supported by the National Natural Science Foundation of China under Grant 62271428. (*Corresponding author: Feng Han*.)

Zhen Guan is with the School of Science, Tianjin University of Technology, Tianjin 300384, China (e-mail: zguan@email.tjut.edu.cn).

Jiawen Li is with the School of Electronic and Information Engineering, Guangxi Normal University, Guangxi 541004, China (e-mail: jiawenli@mailbox.gxnu.edu.cn).

Feng Han is with the School of Computing and Information Technology, Great Bay University, Guangdong 523000, China, and also with the Institute of Electromagnetics and Acoustics, Xiamen University, Xiamen 361005, China (e-mail: feng.han@gbu.edu.cn; feng.han@xmu.edu.cn).

Color versions of one or more figures in this article are available at <https://doi.org/10.1109/TMTT.2023.3320733>.

Digital Object Identifier 10.1109/TMTT.2023.3320733

propagation direction, its amplitude, phase, polarization, and other parameters [2]. Several numerical methods, such as finite-element method (FEM) [3], spectral-element method (SEM) [4], finite-difference time domain (FDTD) [5], and method of moments (MoM) [6], have been proposed to efficiently solve the EM scattering problems. They have also been successfully applied to geophysical exploration [7], microwave imaging [8], subsurface detection [9], periodic structure EM scattering evaluation [10], and so on.

Scattering by multilayered 2-D cylindrical structures is another typical application that has received intensive attention in recent years due to its wide applications in geophysical borehole detection, oil well logging, waveguide as well as artificial EM material design [11], [12], and so on. For example, in the transient EM nondestructive inspection via downhole casings, the transmitting and receiving coils are usually placed inside multicylindrically layered structures within which each layer has distinct permittivity, conductivity, and permeability [13]. In the nondestructive testing of oil and gas well casing, the downhole pulsed eddy-current system is also multicylindrically modeled to rapidly and accurately acquire the wide-frequency-range measurement data [14]. On the other hand, researchers have contributed a lot to the computation of Green’s functions for multilayered cylindrical structures, which were applied to the layout of cylindrical microstrip antennas filled with certain dielectric materials [15], to the fast analysis of the radiation characteristics of parallel-plate cylindrical Luneberg lens antennas [16], and to the response simulation of multicomponent induction well logging [17]. Another popular application for the EM analysis of multilayered cylindrical structures in recent years is the metamaterial design to realize certain EM functions, e.g., cloaking. In [18], detailed formulas are derived to compute the EM scattering by cylindrical metasurfaces, which have arbitrary cross sections but are able to form 2-D porous cavities to achieve penetrable cloaking. In [19], a model-based approach is proposed to analyze the invisibility property of multilayered cylinders, which are filled by uniaxially anisotropic materials with spatial variations of constitutive parameters. Later studies show that even multilayered isotropic dielectric cylinders can also achieve the shielding effect as long as reasonable medium parameters and layer thickness are adopted [20]. Besides these

contributions, pioneers have also conducted a lot of research on EM wave scattering from cylinders filled with composite materials, e.g., metal cylinders covered by plasma layers or other dielectrics [21], [22], [23].

In view of the aforementioned wide and important applications of EM scattering by multilayered cylindrical structures in different areas, researchers have proposed a series of analytical or numerical methods to precisely compute the scattered fields. The most straightforward analytical method is to approximate arbitrary EM fields inside a cylindrically multilayered medium to be the summation of a series of cylindrical vector wave functions in the spectral domain [24], [25], which has been applied to the computation of scattering from open-ended circular cavities with cylindrically periodic terminations [26]. Unfortunately, the summation of cylindrical vector basis functions suffers from extreme arguments or high orders, which is especially severe when computing EM scattering from electrically large cylinders [27]. Most numerical methods can overcome this deficiency by avoiding directly computing the cylindrically layered Green's functions. For cylinders with homogeneous materials filled, the surface integral equation (SIE) can be directly formed and solved by MoM [28]. However, when the cylinders are inhomogeneous, the whole domain instead of only the surface must be discretized. As a result, the FEM is preferred for solving the scattered EM fields from the cylinders [29]. Another efficient hybrid method to solve EM scattering by inhomogeneous cylinders with arbitrary cross sections is to combine the boundary integration and the FEM. The EM fields on the boundary are modeled by the integral equations and, thus, solved by MoM. By contrast, the interior region is discretized by the finite element, and the EM fields are solved by FEM [30]. Although these numerical methods have become rather mature in the past decades and have been applied to different EM scattering scenarios, the computational cost is restricted by a large number of sampling points per wavelength (PPW) in order to achieve a certain accuracy.

Bojarski [31] developed the fast solution of SIE with low sampling density (SD) for the smooth cylinder scattering of acoustic or EM waves via implementing boundary integration in the spectral domain. Also, this spectral integral method (SIM) was later applied to multilayered cylinder scattering by Schuster [32] and to sound-soft or sound-hard smooth cylinder scattering by Hu [33]. On the other hand, SIM has also been applied to the fast computation of EM scattering by periodic structures [34], by a 2-D cylinder embedded inside a layered medium [35], and by a smooth multilayered body with revolution [36]. In our previous work [37], we have applied SIM to the computation of EM scattering from multilayered magnetodielectric concentric circular cylinders. The 2-D cylinders are infinitely long in the  $\hat{z}$ -direction. The excitation plane wave is transverse magnetic ( $TM_z$ ) polarized and, thus, has the  $E_z$ ,  $H_x$ , and  $H_y$  components. Numerical simulations show that the computation error of SIM for the EM scattering by concentric circular cylinders decreases exponentially with the increase of the SD. Also, an SD with three PPW is able to maintain reliable computational accuracy. In this work, we further extend [37] and apply SIM to the

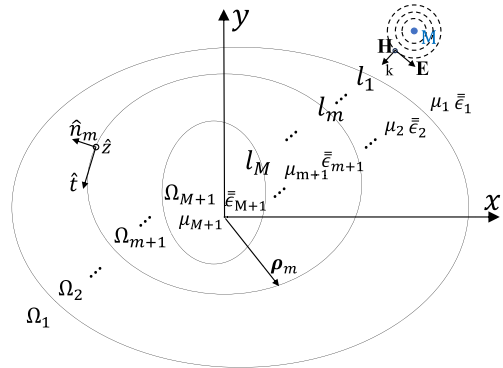


Fig. 1. Multilayered nonconcentric elliptical magnetodielectric cylinders illuminated by an EM wave that is excited by a magnetic dipole source  $M$  and has the  $TE_z$  polarization.

computation of EM scattering by multilayered nonconcentric elliptical magnetodielectric cylinders with transverse electric (TE) illumination. Compared with [37], this work has the following new contributions.

- 1) The multilayered elliptical cylinders are nonconcentric. Each cylinder is allowed to have its own axis ratio. The SIM sampling points in each cylinder circumference are freely chosen.
- 2) The dielectric medium in each elliptical cylinder is allowed to be biaxially anisotropic.
- 3) The excitation sources are magnetic dipoles. The incident wave is  $TE_z$  polarized with the  $H_z$ ,  $E_x$ , and  $E_y$  components.

This article is organized as follows. In Section II, the SIE formulas for EM scattering by nonconcentric multilayered elliptical cylinders with  $TE_z$  illumination are first derived. Then, the SIM formulas are derived based on the SIE results. Meanwhile, 2-D Green's functions for isotropic and biaxially anisotropic media are evaluated. In order to expand Green's functions with Fourier series with lower orders, we must first carry out the singularity subtraction to smoothen them [33]. Finally, the spectral-domain operators are specifically defined, and the discretized algebraic equations are formulated. In Section III, two numerical examples are given to validate the correctness, efficiency, and cost of SIM for computing EM scattering from nonconcentric multilayered elliptical cylinders with isotropic and anisotropic materials, respectively. In Section IV, conclusions are drawn, and discussions are presented.

## II. METHODS

In this section, the SIEs for multilayered nonconcentric elliptical cylinders illuminated by a  $TE_z$  wave are first derived. Then, by expanding both the magnetic fields and Green's functions with Fourier series in multiple elliptical boundaries, we obtain the multilayered spectral integral equations. Finally, the discretized matrix-form equations are formed.

### A. 2-D SIEs for Multilayered Homogeneous Elliptical Cylinders With TE Illumination

As shown in Fig. 1, it is assumed that there are totally  $M$  nonconcentric elliptical cylindrical boundaries and  $M + 1$

homogeneous materials. Their dielectric parameters from the outermost one to the innermost one are recorded as  $(\mu_1, \bar{\epsilon}_1), \dots, (\mu_{M+1}, \bar{\epsilon}_{M+1})$  where

$$\bar{\epsilon}_m = \begin{bmatrix} \epsilon_{xm} & 0 \\ 0 & \epsilon_{ym} \end{bmatrix} + \frac{1}{j\omega\epsilon_0} \begin{bmatrix} \sigma_{xm} & 0 \\ 0 & \sigma_{ym} \end{bmatrix} \quad (1)$$

is the complex relative permittivity in the region  $\Omega_m$ . The tensor is used to denote the 2-D biaxial anisotropy. Suppose an EM wave with  $\text{TE}_z$  polarization and  $\mathbf{E}^{\text{inc}} = \hat{x}E_x^{\text{inc}} + \hat{y}E_y^{\text{inc}}$  and  $\mathbf{H}^{\text{inc}} = \hat{z}H_z^{\text{inc}}$  impinges on the outermost boundary of the cylinders. According to the surface equivalence theorem, this EM scattering scenario can be described by the external and internal state equations

$$\begin{aligned} \mathbf{H}_m^{\text{inc}} &= \mathbf{H}_m(\boldsymbol{\rho}_m) \\ &- \oint_{l_m} \bar{\mathbf{G}}_{\mathbf{HJ}}(\mu_m, \bar{\epsilon}_m, \boldsymbol{\rho}_m, \boldsymbol{\rho}'_m) \cdot \mathbf{J}_{m,o}(\boldsymbol{\rho}'_m) dt' \\ &- \oint_{l_m} \bar{\mathbf{G}}_{\mathbf{HM}}(\mu_m, \bar{\epsilon}_m, \boldsymbol{\rho}_m, \boldsymbol{\rho}'_m) \cdot \mathbf{M}_{m,o}(\boldsymbol{\rho}'_m) dt' \\ &- \oint_{l_{m-1}} \bar{\mathbf{G}}_{\mathbf{HJ}}(\mu_m, \bar{\epsilon}_m, \boldsymbol{\rho}_m, \boldsymbol{\rho}'_{m-1}) \cdot \mathbf{J}_{m-1,i}(\boldsymbol{\rho}'_{m-1}) dt' \\ &- \oint_{l_{m-1}} \bar{\mathbf{G}}_{\mathbf{HM}}(\mu_m, \bar{\epsilon}_m, \boldsymbol{\rho}_m, \boldsymbol{\rho}'_{m-1}) \cdot \mathbf{M}_{m-1,i}(\boldsymbol{\rho}'_{m-1}) dt' \end{aligned} \quad (2a)$$

$$\begin{aligned} \mathbf{0} &= \mathbf{H}_m(\boldsymbol{\rho}_m) \\ &- \oint_{l_m} \bar{\mathbf{G}}_{\mathbf{HJ}}(\mu_{m+1}, \bar{\epsilon}_{m+1}, \boldsymbol{\rho}_m, \boldsymbol{\rho}'_m) \cdot \mathbf{J}_{m,i}(\boldsymbol{\rho}'_m) dt' \\ &- \oint_{l_m} \bar{\mathbf{G}}_{\mathbf{HM}}(\mu_{m+1}, \bar{\epsilon}_{m+1}, \boldsymbol{\rho}_m, \boldsymbol{\rho}'_m) \cdot \mathbf{M}_{m,i}(\boldsymbol{\rho}'_m) dt' \\ &- \oint_{l_{m+1}} \bar{\mathbf{G}}_{\mathbf{HJ}}(\mu_{m+1}, \bar{\epsilon}_{m+1}, \boldsymbol{\rho}_m, \boldsymbol{\rho}'_{m+1}) \cdot \mathbf{J}_{m+1,o}(\boldsymbol{\rho}'_{m+1}) dt' \\ &- \oint_{l_{m+1}} \bar{\mathbf{G}}_{\mathbf{HM}}(\mu_{m+1}, \bar{\epsilon}_{m+1}, \boldsymbol{\rho}_m, \boldsymbol{\rho}'_{m+1}) \cdot \mathbf{M}_{m+1,o}(\boldsymbol{\rho}'_{m+1}) dt' \end{aligned} \quad (2b)$$

where  $m = 1, \dots, M$ .  $\mathbf{H}_m^{\text{inc}}$  and  $\mathbf{H}_m$  are, respectively, the incident and total magnetic fields in the  $m$ th boundary.  $\bar{\mathbf{G}}_{\mathbf{HJ}}$  and  $\bar{\mathbf{G}}_{\mathbf{HM}}$  are 2-D Green's functions whose expressions are given in Appendixes A and B for both isotropic and biaxially anisotropic materials. The  $\boldsymbol{\rho}_m$  and  $\boldsymbol{\rho}'_m$ , respectively, denote the field point position and equivalent source point position in the  $m$ th boundary.  $\mathbf{J}_{m,o}$  and  $\mathbf{J}_{m,i}$ , respectively, denote the equivalent electric current in the outside and inside sides of the  $m$ th boundary. In a similar way,  $\mathbf{M}_{m,o}$  and  $\mathbf{M}_{m,i}$ , respectively, denote the equivalent magnetic current in the outside and inside sides of the  $m$ th boundary. Finally, it should be emphasized that only  $\mathbf{H}_1^{\text{inc}} = \mathbf{H}^{\text{inc}}$  and  $\mathbf{H}_2^{\text{inc}}, \dots, \mathbf{H}_M^{\text{inc}}$  are zero in our problem. Meanwhile, the integrals  $\oint_{l_0}$  and  $\oint_{l_{M+1}}$  are automatically set as zero, since the zeroth and  $(M+1)$ th boundaries do not exist. Because the tangential components of the electric or magnetic fields in each boundary are continuous, we have

$$\mathbf{J}_{m,o} = -\mathbf{J}_{m,i} = \hat{n}'_m \times \mathbf{H}_m \quad (3a)$$

$$\mathbf{M}_{m,o} = -\mathbf{M}_{m,i} = -\hat{n}'_m \times \mathbf{E}_m \quad (3b)$$

where  $\hat{n}'_m = \hat{x}n'_{xm} + \hat{y}n'_{ym}$  is the outward unit normal vector in the  $m$ th boundary. Equation (3), therefore, can be rewritten as follows:

$$J_{xm,o} = -J_{xm,i} = n'_{ym} H_{zm} \quad (4a)$$

$$J_{ym,o} = -J_{ym,i} = -n'_{xm} H_{zm} \quad (4b)$$

$$M_{zm,o} = -M_{zm,i} = -E_{tm} \quad (4c)$$

where  $H_{zm}$  is the  $\hat{z}$  component of the total magnetic field in the  $m$ th boundary, while  $E_{tm}$  is the tangential component of the total electric field. In order to facilitate further derivation, we first define the new variable  $\bar{E}_t$  and the new symbolic operators  $\mathcal{K}_{pq}^h$  and  $\mathcal{L}_{pq}^h$

$$\bar{E}_t = \frac{1}{\eta_0} E_t \quad (5a)$$

$$\begin{aligned} \mathcal{K}_{pq}^{h,s}\{H_{zq}\} &= \oint_{l_q} G_{HJ}^{zx}(\mu_s, \bar{\epsilon}_s, \boldsymbol{\rho}_p, \boldsymbol{\rho}'_q) n'_{yq} \{H_{zq}(\boldsymbol{\rho}'_q)\} dt' \\ &- \oint_{l_q} G_{HJ}^{zy}(\mu_s, \bar{\epsilon}_s, \boldsymbol{\rho}_p, \boldsymbol{\rho}'_q) n'_{xq} \{H_{zq}(\boldsymbol{\rho}'_q)\} dt' \end{aligned} \quad (5b)$$

$$\mathcal{L}_{pq}^{h,s}\{\bar{E}_{tq}\} = -\eta_0 \oint_{l_q} G_{HM}^{zz}(\mu_s, \bar{\epsilon}_s, \boldsymbol{\rho}_p, \boldsymbol{\rho}'_q) \{\bar{E}_{tq}(\boldsymbol{\rho}'_q)\} dt' \quad (5c)$$

where  $\eta_0$  denotes the intrinsic impedance of the free space, the superscript  $h$  means the magnetic field is evaluated,  $s = 1, \dots, M+1$  is the material index, the subscript  $p = 1, \dots, M$  is the index of the boundary in which the field point locates,  $q = 1, \dots, M$  is the index of the boundary in which the equivalent source point locates, and  $\oint$  is the principal-value integral with the singularity extracted when  $p = q$  and  $\boldsymbol{\rho}_p$  and  $\boldsymbol{\rho}'_q$  overlap in the  $q$ th boundary. Note the scaling of the electric field in (5a) is to guarantee that the solved electric field values and magnetic field values are commensurate.

Then, by substituting (4) and  $\bar{\mathbf{G}}_{\mathbf{HJ}}$  as well as  $\bar{\mathbf{G}}_{\mathbf{HM}}$  given in Appendixes A and B into (2), considering the singularity extraction when the source point and field point overlap in the  $m$ th boundary [38], and making use of the definitions given in (5), we obtain the compact form of the state equation (6) for the  $m$ th boundary, which is shown at the bottom of the next page. Finally, we let  $m$  change from 1 to  $M$ , assemble all  $M$  state equations similar to (6) together, and obtain the multilayered boundary integral equations with the unknowns  $H_{z,1,\dots,M}$  and  $\bar{E}_{t,m=1,\dots,M}$ , which can be easily discretized and solved by MoM [28].

The scattered magnetic fields at the receiver array can be obtained by applying the operators  $\mathcal{K}^h$  and  $\mathcal{L}^h$  in (5) to the total field vectors on the boundaries if we replace  $\boldsymbol{\rho}_p$  with the receiver position  $\boldsymbol{\rho}_r$  and also replace  $\oint$  with  $\oint$ , since the receivers do not locate in the layer boundaries. However, in order to compute the scattered electric fields at the receiver array, we need to define the new symbolic operators  $\mathcal{K}_{rq}^{ex}$ ,  $\mathcal{K}_{rq}^{ey}$ ,  $\mathcal{L}_{rq}^{ex}$ , and  $\mathcal{L}_{rq}^{ey}$

$$\mathcal{K}_{rq}^{ex,s}\{H_{zq}\} = \oint_{l_q} G_{EJ}^{xx}(\mu_s, \bar{\epsilon}_s, \boldsymbol{\rho}_r, \boldsymbol{\rho}'_q) n'_{yq} \{H_{zq}(\boldsymbol{\rho}'_q)\} dt' \quad (5d)$$

$$-\oint_{l_q} G_{EJ}^{xy}(\mu_s, \bar{\epsilon}_s, \rho_r, \rho'_q) n'_{xq} \{H_{zq}(\rho'_q)\} dt' \quad (7a)$$

$$\begin{aligned} \mathcal{K}_{rq}^{ey,s} \{H_{zq}\} &= \oint_{l_q} G_{EJ}^{yx}(\mu_s, \bar{\epsilon}_s, \rho_r, \rho'_q) n'_{yq} \{H_{zq}(\rho'_q)\} dt' \\ &\quad - \oint_{l_q} G_{EJ}^{yy}(\mu_s, \bar{\epsilon}_s, \rho_r, \rho'_q) n'_{xq} \{H_{zq}(\rho'_q)\} dt' \end{aligned} \quad (7b)$$

$$\mathcal{L}_{rq}^{ex,s} \{\bar{E}_{tq}\} = -\eta_0 \oint_{l_q} G_{EM}^{xz}(\mu_s, \bar{\epsilon}_s, \rho_r, \rho'_q) \{\bar{E}_{tq}(\rho'_q)\} dt' \quad (7c)$$

$$\mathcal{L}_{rq}^{ey,s} \{\bar{E}_{tq}\} = -\eta_0 \oint_{l_q} G_{EM}^{yz}(\mu_s, \bar{\epsilon}_s, \rho_r, \rho'_q) \{\bar{E}_{tq}(\rho'_q)\} dt' \quad (7d)$$

where  $s$  is the index of the material in which the receiver locates, the superscript  $ex$  means the  $\hat{x}$  component of the electric field, while  $ey$  means the  $\hat{y}$  component of the electric field, and the subscript  $r$  denotes the receiver. In addition, the scattered fields at a certain receiver are only contributed by the equivalent current in two adjacent boundaries.

The operators defined in (5) and (7) are all in the spatial domain. The MoM to solve the multilayered SIEs is also implemented in the spatial domain. In this work, we adopt the pulse basis and point matching method. Because it is rather trivial, MoM will not be discussed here. Usually, at least a ten-PPW SD for the discretization and implementation of MoM is required in the elliptical boundaries to maintain reliable numerical accuracy [28]. Unfortunately, this high SD will lead to an unaffordable computational cost when the elliptical scatterer has a large electrical size and numerous layer boundaries. One of the feasible methods to lower the computational cost is to implement surface integrals in the spectral domain. In other words, we expand the operators defined in (5) with Fourier series and directly solve for the Fourier coefficients of  $H_z$  and  $\bar{E}_t$ . Consequently, the necessary SD for the discretization along the elliptical boundaries is expected to be significantly lowered according to the Nyquist sampling theorem. This will be discussed in detail in the following.

### B. SIM for EM Scattering by 2-D Multilayered Elliptical Cylinders With TE Illumination

Since the EM fields along the smooth cylindrical boundaries are periodic functions of the azimuthal angle  $\theta$  with the cycle of  $2\pi$ , they can be approximated by the truncated Fourier

series as follows:

$$H_{zm}(\theta) = \sum_{n=-\frac{N_m}{2}}^{\frac{N_m}{2}-1} \tilde{H}_{zm}^n e^{-jn\theta} \quad (8a)$$

$$\bar{E}_{tm}(\theta) = \sum_{n=-\frac{N_m}{2}}^{\frac{N_m}{2}-1} \tilde{\bar{E}}_{tm}^n e^{-jn\theta} \quad (8b)$$

where  $\theta$  is the azimuthal angle for the  $m$ th elliptical boundary,  $(N_m/2)$  is the order of the Fourier series, and  $\tilde{H}_{zm}^n$  and  $\tilde{\bar{E}}_{tm}^n$  are the corresponding  $n$ th Fourier coefficients. We then redefine the integral along the  $m$ th elliptical boundary  $\oint_{l_m} \{\cdot\} dt' = \int_0^{2\pi} \{\cdot\} (d\rho'_m/d\theta') d\theta'$ , apply the operators  $\mathcal{K}_{mm}^{h,m}$  and  $\mathcal{L}_{mm}^{h,m}$ , respectively, to the boundary fields  $H_{zm}$  and  $\bar{E}_{tm}$  in (8), exchange the order of summation and integration, and, finally, write the spectral-domain operation as follows:

$$\begin{aligned} \tilde{\mathcal{K}}_{mm}^{h,m} \{H_{zm}\} &= \sum_{n=-\frac{N_m}{2}}^{\frac{N_m}{2}-1} \tilde{H}_{zm}^n \int_0^{2\pi} e^{-jn\theta'} G_{HJ}^{zx}(\theta_m, \theta'_m) n'_{ym} \left| \frac{d\rho'_m}{d\theta'} \right| d\theta' \\ &\quad - \sum_{n=-\frac{N_m}{2}}^{\frac{N_m}{2}-1} \tilde{H}_{zm}^n \int_0^{2\pi} e^{-jn\theta'} G_{HJ}^{zy}(\theta_m, \theta'_m) n'_{xm} \left| \frac{d\rho'_m}{d\theta'} \right| d\theta' \end{aligned} \quad (9a)$$

$$\begin{aligned} \tilde{\mathcal{L}}_{mm}^{h,m} \{\bar{E}_{tm}\} &= - \sum_{n=-\frac{N_m}{2}}^{\frac{N_m}{2}-1} \tilde{\bar{E}}_{tm}^n \eta_0 \int_0^{2\pi} e^{-jn\theta'} G_{HM}^{zz}(\theta_m, \theta'_m) \left| \frac{d\rho'_m}{d\theta'} \right| d\theta' \end{aligned} \quad (9b)$$

where  $\theta_m$  and  $\theta'_m$  are, respectively, the field point and the equivalent source point in the  $m$ th boundary but are denoted by the azimuthal angle, and  $n'_{x,m}$  and  $n'_{y,m}$  also vary with  $\theta'$ . The integrals in (9) with respect to the azimuth angle are actually to compute the  $n$ th Fourier coefficients of Green's functions multiplied with some variables. It is well known that Green's functions usually show strong singularity when  $\theta_m$  and  $\theta'_m$  approach, which will lead to the generation of high-order Fourier coefficients. In order to suppress the high-order components, we take the same smoothening procedure given in [33], since Green's functions in this work are also combinations of the first-order and second-order Hankel functions. Therefore, we can rewrite three Green's functions in (9) as the summation of smooth terms and logarithmic terms. They are, respectively, expressed as follows:

$$\begin{aligned} G_{HJ}^{zx}(\theta_m, \theta'_m) &= \bar{G}_{HJ}^{zx}(\theta_m, \theta'_m) \\ &\quad + C_{HJ}^{zx}(\theta_m, \theta'_m) \cdot \frac{2}{\pi j} \ln \left| 2 \sin \left( \frac{\theta_m - \theta'_m}{2} \right) \right| \end{aligned}$$

$$\begin{bmatrix} -\mathcal{K}_{m,m-1}^{h,m} & -\mathcal{L}_{m,m-1}^{h,m} & \frac{1}{2} - \mathcal{K}_{mm}^{h,m} & -\mathcal{L}_{mm}^{h,m} \\ 0 & 0 & \frac{1}{2} - \mathcal{K}_{mm}^{h,m+1} & -\mathcal{L}_{mm}^{h,m+1} \\ -\mathcal{K}_{m,m+1}^{h,m+1} & -\mathcal{L}_{m,m+1}^{h,m+1} & 0 & 0 \end{bmatrix} \begin{bmatrix} H_{z,m-1} \\ \bar{E}_{t,m-1} \\ H_{zm} \\ \bar{E}_{tm} \\ H_{z,m+1} \\ \bar{E}_{t,m+1} \end{bmatrix} = \begin{bmatrix} H_{zm}^{\text{inc}} \\ 0 \end{bmatrix} \quad (6)$$

$$\cdot J_1(KR) \quad (10a)$$

$$\begin{aligned} G_{HJ}^{zy}(\theta_m, \theta'_m) &= \overline{G}_{HJ}^{zy}(\theta_m, \theta'_m) \\ &+ C_{HJ}^{zy}(\theta_m, \theta'_m) \cdot \frac{2}{\pi j} \ln \left| 2 \sin \left( \frac{\theta_m - \theta'_m}{2} \right) \right| \\ &\cdot J_1(KR) \end{aligned} \quad (10b)$$

$$\begin{aligned} G_{HM}^{zz}(\theta_m, \theta'_m) &= \overline{G}_{HM}^{zz}(\theta_m, \theta'_m) \\ &+ C_{HM}^{zz} \cdot \frac{2}{\pi j} \ln \left| 2 \sin \left( \frac{\theta_m - \theta'_m}{2} \right) \right| \cdot J_0(KR) \end{aligned} \quad (10c)$$

where  $KR = k_m |\rho_m(\theta_m) - \rho'_m(\theta'_m)|$  for the isotropic medium but is equal to  $k_0(\mu_m)^{1/2}([\epsilon_{ym}(x(\theta_m) - x'(\theta'_m))^2 + \epsilon_{xm}(y(\theta_m) - y'(\theta'_m))^2])^{1/2}$  for the biaxially anisotropic medium. The three coefficients in front of the logarithmic terms are expressed as follows:

$$C_{HJ}^{zx} = -\frac{jk_m}{4} \sin[\phi(\theta_m, \theta'_m)] \quad (11a)$$

$$C_{HJ}^{zy} = \frac{jk_m}{4} \cos[\phi(\theta_m, \theta'_m)] \quad (11b)$$

$$C_{HM}^{zz} = -\frac{\omega \epsilon_0 \epsilon_m}{4} \quad (11c)$$

for the isotropic medium but are expressed as follows:

$$C_{HJ}^{zx} = -\frac{jk_{xm}}{4} \left( \frac{\epsilon_{ym}}{\epsilon_{xm}} \right)^{\frac{1}{2}} \sin[\phi_x(\theta_m, \theta'_m)] \quad (12a)$$

$$C_{HJ}^{zy} = \frac{jk_{ym}}{4} \left( \frac{\epsilon_{xm}}{\epsilon_{ym}} \right)^{\frac{1}{2}} \cos[\phi_y(\theta_m, \theta'_m)] \quad (12b)$$

$$C_{HM}^{zz} = -\frac{\omega \epsilon_0 \sqrt{\epsilon_{xm} \epsilon_{ym}}}{4} \quad (12c)$$

for the biaxially anisotropic medium. By substituting (10) into (9), we come to the final forms of the operators

$$\begin{aligned} &\tilde{\mathcal{K}}_{mm}^{h,m}\{H_{zm}\} \\ &= \sum_{n=-\frac{N_m}{2}}^{\frac{N_m}{2}-1} \tilde{H}_{zm}^n \int_0^{2\pi} e^{-jn\theta'} \left( \overline{G}_{HJ}^{zx}(\theta_m, \theta'_m) n'_{ym} \left| \frac{d\rho'_m}{d\theta'} \right| \right. \\ &\quad \left. + \frac{2}{\pi j} \ln \left| 2 \sin \left( \frac{\theta_m - \theta'_m}{2} \right) \right| \right. \\ &\quad \times J_1(KR) C_{HJ}^{zx} n'_{ym} \left| \frac{d\rho'_m}{d\theta'} \right| \right) d\theta' \\ &- \sum_{n=-\frac{N_m}{2}}^{\frac{N_m}{2}-1} \tilde{H}_{zm}^n \int_0^{2\pi} e^{-jn\theta'} \left( \overline{G}_{HJ}^{zy}(\theta_m, \theta'_m) n'_{xm} \left| \frac{d\rho'_m}{d\theta'} \right| \right. \\ &\quad \left. + \frac{2}{\pi j} \ln \left| 2 \sin \left( \frac{\theta_m - \theta'_m}{2} \right) \right| \right. \\ &\quad \times J_1(KR) C_{HJ}^{zy} n'_{xm} \left| \frac{d\rho'_m}{d\theta'} \right| \right) d\theta' \end{aligned} \quad (13a)$$

$$\begin{aligned} &\tilde{\mathcal{L}}_{mm}^{h,m}\{\bar{E}_{tm}\} \\ &= - \sum_{n=-\frac{N_m}{2}}^{\frac{N_m}{2}-1} \tilde{E}_{tm}^n \eta_0 \int_0^{2\pi} e^{-jn\theta'} \left( \overline{G}_{HM}^{zz}(\theta_m, \theta'_m) \left| \frac{d\rho'_m}{d\theta'} \right| \right. \end{aligned}$$

$$\begin{aligned} &+ \frac{2}{\pi j} C_{HM}^{zz} \ln \left| 2 \sin \left( \frac{\theta_m - \theta'_m}{2} \right) \right| \\ &\times J_0(KR) \left| \frac{d\rho'_m}{d\theta'} \right| \right) d\theta'. \end{aligned} \quad (13b)$$

Two points must be emphasized here. First, the aforementioned smoothening procedure is valid for the external state equation of the  $m$ th boundary. For the internal state equation described by the operators  $\tilde{\mathcal{K}}_{mm}^{h,m+1}$  and  $\tilde{\mathcal{L}}_{mm}^{h,m+1}$ , the EM wave propagates in the  $(m+1)$ th medium. Equations (10)–(12) still can be used to construct them as long as we replace  $k_m$  with  $k_{m+1}$ ,  $k_{xm}$  with  $k_{x,m+1}$ ,  $k_{ym}$  with  $k_{y,m+1}$ ,  $\epsilon_{xm}$  with  $\epsilon_{x,m+1}$ , and  $\epsilon_{ym}$  with  $\epsilon_{y,m+1}$ . Second, when we construct the spectral-domain operators  $\tilde{\mathcal{K}}_{m,m-1}^{h,m}$ ,  $\tilde{\mathcal{K}}_{m,m+1}^{h,m}$ ,  $\tilde{\mathcal{L}}_{m,m-1}^{h,m}$ , and  $\tilde{\mathcal{L}}_{m,m+1}^{h,m}$  to evaluate the magnetic fields at the  $m$ th boundary contributed by the equivalent current source at two adjacent boundaries, the aforementioned smoothening procedure becomes unnecessary. In this situation, the singularity of Green's functions is significantly weakened, since the source points and field points locate in different elliptical boundaries. Consequently, we can directly construct these four spectral-domain operators using similar definitions to (9) but replace the medium dielectric parameters in the  $m$ th layer with those in the  $(m-1)$ th or  $(m+1)$ th layer when computing Green's functions,  $\rho_m$  with  $\rho_{m-1}$  or  $\rho_{m+1}$ ,  $\hat{n}'_m$  with  $\hat{n}'_{m-1}$  or  $\hat{n}'_{m+1}$ ,  $\tilde{H}_{zm}$  with  $\tilde{H}_{z,m-1}$  or  $\tilde{H}_{z,m+1}$ , and  $\tilde{E}_{tm}$  with  $\tilde{E}_{t,m-1}$  or  $\tilde{E}_{t,m+1}$ .

Once the spectral-domain operators  $\tilde{\mathcal{K}}$  and  $\tilde{\mathcal{L}}$  are constructed, we can also derive the spectral-domain state equation similar to (6) for the  $m$ th boundary. Finally, we let  $m$  change from 1 to  $M$ , assemble all  $M$  spectral-domain state equations together, and obtain the multilayered spectral integral equations with the unknowns  $\tilde{H}_{zm}$  and  $\tilde{E}_{tm}$  with  $m = 1, \dots, M$ . In order to evaluate the scattered EM fields recorded by a certain receiver, we assume that it locates at a fictitious circular boundary, and its position is denoted by  $\theta_r$ . The spectral-domain operators  $\tilde{\mathcal{K}}_{rq}^{h,s}$  and  $\tilde{\mathcal{L}}_{rq}^{h,s}$  can be constructed similar to (9) if we replace  $\theta_m$  with  $\theta_r$ ,  $\theta'_m$  with  $\theta'_q$ ,  $\rho'_m$  with  $\rho'_q$ ,  $\hat{n}'_m$  with  $\hat{n}'_q$ ,  $\tilde{H}_{zm}$  with  $\tilde{H}_{zq}$ , and  $\tilde{E}_{tm}$  with  $\tilde{E}_{tq}$ , and compute Green's functions using the dielectric parameters of the  $s$ th medium. The spectral-domain operators  $\tilde{\mathcal{K}}_{rq}^{ex,s}$ ,  $\tilde{\mathcal{K}}_{rq}^{ey,s}$ ,  $\tilde{\mathcal{L}}_{rq}^{ex,s}$ , and  $\tilde{\mathcal{L}}_{rq}^{ey,s}$  can be constructed following the similar procedure but referring to (7). Finally, it should be emphasized that the smoothening procedure in (10)–(12) is unnecessary for the operators used to compute the scattered fields.

### C. Discretization of the 2-D Spectral Integral Equations

In the spectral-domain operators  $\tilde{\mathcal{K}}$  and  $\tilde{\mathcal{L}}$ , both the field point denoted by  $\theta$  and the source point denoted by  $\theta'$  vary continuously along the elliptical circumference. For the  $m$ th boundary, we can discretize it

$$\theta_{mi} = 2\pi \left( i + \frac{1}{2} \right) / N_m, \quad i = 0, 1, \dots, N_m - 1 \quad (14a)$$

$$\theta'_{mi'} = 2\pi i' / N_m, \quad i' = 0, 1, \dots, N_m - 1 \quad (14b)$$

where the source point and the field point have misaligned half grid in the circumference to avoid evaluating the Bessel

functions when  $\theta = \theta'$ . In addition, the discretization point number must remain the same as the Fourier series order used in (8), since only in this way can the system matrix be square. Then, the integral  $\int_0^{2\pi} \{\} d\theta'$  to compute the Fourier coefficients in (13) can be approximated by algebraic summation. Thus, for a certain field point  $\theta_{mi}$ , we define the coefficients

$$\begin{aligned} 2\pi f_{mi,m}^n &= \int_0^{2\pi} e^{-jn\theta'} \bar{G}_{HJ}^{zx}(\theta_{mi}, \theta'_m) n'_{ym} \left| \frac{d\boldsymbol{\rho}'_m}{d\theta'} \right| d\theta' \\ &\approx \frac{2\pi}{N_m} \sum_{i'=0}^{N_m-1} e^{-jn\theta'_{mi'}} \bar{G}_{HJ}^{zx}(\theta_{mi}, \theta'_{mi'}) n'_{ym} \left| \frac{d\boldsymbol{\rho}'_m}{d\theta'}(\theta'_{mi'}) \right| \end{aligned} \quad (15a)$$

$$\begin{aligned} 2\pi g_{mi,m}^n &= \int_0^{2\pi} e^{-jn\theta'} \bar{G}_{HJ}^{zy}(\theta_{mi}, \theta'_m) n'_{xm} \left| \frac{d\boldsymbol{\rho}'_m}{d\theta'} \right| d\theta' \\ &\approx \frac{2\pi}{N_m} \sum_{i'=0}^{N_m-1} e^{-jn\theta'_{mi'}} \bar{G}_{HJ}^{zy}(\theta_{mi}, \theta'_{mi'}) n'_{xm} \left| \frac{d\boldsymbol{\rho}'_m}{d\theta'}(\theta'_{mi'}) \right| \end{aligned} \quad (15b)$$

$$\begin{aligned} 2\pi h_{mi,m}^n &= \int_0^{2\pi} e^{-jn\theta'} \bar{G}_{HM}^{zz}(\theta_{mi}, \theta'_m) \left| \frac{d\boldsymbol{\rho}'_m}{d\theta'} \right| d\theta' \\ &\approx \frac{2\pi}{N_m} \sum_{i'=0}^{N_m-1} e^{-jn\theta'_{mi'}} \bar{G}_{HM}^{zz}(\theta_{mi}, \theta'_{mi'}) \left| \frac{d\boldsymbol{\rho}'_m}{d\theta'}(\theta'_{mi'}) \right| \end{aligned} \quad (15c)$$

where the subscript  $(mi, m)$  means the equivalent source locating at the  $m$ th boundary contributes to the  $i$ th discretized field point at the  $m$ th boundary. Following the similar procedure, we can also define Fourier coefficients  $f_{mi,m-1}^n, g_{mi,m-1}^n, h_{mi,m-1}^n, f_{mi,m+1}^n, g_{mi,m+1}^n$ , and  $h_{mi,m+1}^n$ . Note, in these cases, that the smooth  $\bar{G}$  in (15) must be replaced with original the Green's function  $G$ , since the smoothening procedure in (10)–(12) is unnecessary when the source points and field points locate in different elliptical boundaries. The other three remaining integral terms in (13) are actually to compute the Fourier coefficients of the multiplication of the logarithmic term and the Bessel function term. They can be evaluated by the convolution of their respective Fourier coefficients. Therefore, we first define the Fourier coefficients of Bessel function terms

$$\begin{aligned} 2\pi \hat{u}_{mi,m}^n &= \int_0^{2\pi} e^{-jn\theta'} J_1(KR) C_{HJ}^{zx} n'_{ym} \left| \frac{d\boldsymbol{\rho}'_m}{d\theta'} \right| d\theta' \\ &\approx \frac{2\pi}{N_m} \sum_{i'=0}^{N_m-1} e^{-jn\theta'_{mi'}} J_1(KR) C_{HJ}^{zx} n'_{ym} \left| \frac{d\boldsymbol{\rho}'_m}{d\theta'}(\theta'_{mi'}) \right| \end{aligned} \quad (16a)$$

$$\begin{aligned} 2\pi \hat{v}_{mi,m}^n &= \int_0^{2\pi} e^{-jn\theta'} J_1(KR) C_{HJ}^{zy} n'_{xm} \left| \frac{d\boldsymbol{\rho}'_m}{d\theta'} \right| d\theta' \\ &\approx \frac{2\pi}{N_m} \sum_{i'=0}^{N_m-1} e^{-jn\theta'_{mi'}} J_1(KR) C_{HJ}^{zy} n'_{xm} \left| \frac{d\boldsymbol{\rho}'_m}{d\theta'}(\theta'_{mi'}) \right| \end{aligned} \quad (16b)$$

$$2\pi \hat{w}_{mi,m}^n = \int_0^{2\pi} e^{-jn\theta'} C_{HM}^{zz} J_0(KR) \left| \frac{d\boldsymbol{\rho}'_m}{d\theta'} \right| d\theta' \quad (16c)$$

$$\approx \frac{2\pi}{N_m} \sum_{i'=0}^{N_m-1} e^{-jn\theta'_{mi'}} C_{HM}^{zz} J_0(KR) \left| \frac{d\boldsymbol{\rho}'_m}{d\theta'}(\theta'_{mi'}) \right|. \quad (16c)$$

Then, we expand the logarithmic term in (13) with Fourier coefficients in the  $m$ th elliptical boundary

$$\begin{aligned} \ln \left| 2 \sin \left( \frac{\theta_m - \theta'_m}{2} \right) \right| &= \sum_{n=-\infty}^{\infty} a_n e^{jn(\theta_m - \theta'_m)} \\ &= \sum_{n=-\infty}^{\infty} a_n e^{jn\theta_m} \cdot e^{-jn\theta'_m} \end{aligned} \quad (17)$$

where  $a_0 = 0$ ,  $a_n = -(1/2|n|)$  for  $n \neq 0$ , and  $a_n e^{jn\theta_m}$  is the  $n$ th coefficient. Finally, the three integral terms in (13) for the multiplication of the logarithmic term and the Bessel function term can be, respectively, expressed as the following convolution sums of the aforementioned two groups of Fourier coefficients:

$$\begin{aligned} &\frac{2}{\pi j} \int_0^{2\pi} e^{-jn\theta'} \ln \left| 2 \sin \left( \frac{\theta_m - \theta'_m}{2} \right) \right| J_1 \cdot C_{HJ}^{zx} n'_{ym} \left| \frac{d\boldsymbol{\rho}'_m}{d\theta'} \right| d\theta' \\ &= -4j \sum_{k=-N_m/2}^{N_m/2-1} \hat{u}_{mi,m}^k a_{n-k} e^{j(n-k)\theta_m} \\ &\equiv -4j u_{mi,m}^n \end{aligned} \quad (18a)$$

$$\begin{aligned} &\frac{2}{\pi j} \int_0^{2\pi} e^{-jn\theta'} \ln \left| 2 \sin \left( \frac{\theta_m - \theta'_m}{2} \right) \right| J_1 \cdot C_{HJ}^{zy} n'_{xm} \left| \frac{d\boldsymbol{\rho}'_m}{d\theta'} \right| d\theta' \\ &= -4j \sum_{k=-N_m/2}^{N_m/2-1} \hat{v}_{mi,m}^k a_{n-k} e^{j(n-k)\theta_m} \\ &\equiv -4j v_{mi,m}^n \end{aligned} \quad (18b)$$

$$\begin{aligned} &\frac{2\eta_0}{\pi j} \int_0^{2\pi} e^{-jn\theta'} C_{HM}^{zz} \ln \left| 2 \sin \left( \frac{\theta_m - \theta'_m}{2} \right) \right| J_0(KR) \left| \frac{d\boldsymbol{\rho}'_m}{d\theta'} \right| d\theta' \\ &= -4j \eta_0 \sum_{k=-N_m/2}^{N_m/2-1} \hat{w}_{mi,m}^k a_{n-k} e^{j(n-k)\theta_m} \\ &\equiv -4j \eta_0 w_{mi,m}^n \end{aligned} \quad (18c)$$

where  $i = 0, \dots, N_m - 1$  is the field point index in the  $m$ th elliptical boundary and  $n = -N_m/2, \dots, N_m/2 - 1$  is the order of the Fourier series. The convolution sums can be evaluated by the fast Fourier transform. Details can be found in Sections II–IV of [33] and will not be repeated here. We now update  $\tilde{\mathcal{K}}_{mm}^{h,m}$  and  $\tilde{\mathcal{L}}_{mm}^{h,m}$  in (13) using the definitions given in (15) and (18), construct  $\tilde{\mathcal{K}}_{m,m-1}^{h,m}$ ,  $\tilde{\mathcal{K}}_{m,m+1}^{h,m}$ ,  $\tilde{\mathcal{L}}_{m,m-1}^{h,m}$ , and  $\tilde{\mathcal{L}}_{m,m+1}^{h,m}$  using  $f_{mi,m-1}^n, g_{mi,m-1}^n, h_{mi,m-1}^n, f_{mi,m+1}^n, g_{mi,m+1}^n$ , and  $h_{mi,m+1}^n$ , and, respectively, come to the external and internal discretized spectral-domain integral equations for the  $m$ th elliptical boundary

$$\begin{aligned} &-2\pi \sum_{n=-\frac{N_m-1}{2}}^{\frac{N_m-1}{2}-1} \tilde{H}_{z,m-1}^n (f_{mi,m-1}^n - g_{mi,m-1}^n) \\ &+ 2\pi \eta_0 \sum_{n=-\frac{N_m-1}{2}}^{\frac{N_m-1}{2}-1} \tilde{E}_{t,m-1}^n h_{mi,m-1}^n + \frac{1}{2} \sum_{n=-\frac{N_m}{2}}^{\frac{N_m}{2}-1} \tilde{H}_{zm}^n e^{-jn\theta_m} \end{aligned}$$

$$\begin{aligned}
& -2\pi \sum_{n=-\frac{N_m}{2}}^{\frac{N_m}{2}-1} \tilde{H}_{zm}^n (f_{mi,m}^n - g_{mi,m}^n) \\
& + 4j \sum_{n=-\frac{N_m}{2}}^{\frac{N_m}{2}-1} \tilde{H}_{zm}^n (u_{mi,m}^n - v_{mi,m}^n) \\
& + \eta_0 \sum_{n=-\frac{N_m}{2}}^{\frac{N_m}{2}-1} \tilde{E}_{tm}^n (2\pi h_{mi,m}^n - 4j w_{mi,m}^n) \\
= & H_{zm}^{\text{inc}}(\theta_{mi}) \tag{19a}
\end{aligned}$$

$$\begin{aligned}
& \frac{1}{2} \sum_{n=-\frac{N_m}{2}}^{\frac{N_m}{2}-1} \tilde{H}_{zm}^n e^{-jn\theta_{mi}} - 2\pi \sum_{n=-\frac{N_m}{2}}^{\frac{N_m}{2}-1} \tilde{H}_{zm}^n (f_{mi,m}^n - g_{mi,m}^n) \\
& + 4j \sum_{n=-\frac{N_m}{2}}^{\frac{N_m}{2}-1} \tilde{H}_{zm}^n (u_{mi,m}^n - v_{mi,m}^n) \\
& + \eta_0 \sum_{n=-\frac{N_m}{2}}^{\frac{N_m}{2}-1} \tilde{E}_{tm}^n (2\pi h_{mi,m}^n - 4j w_{mi,m}^n) \\
& - 2\pi \sum_{n=-\frac{N_{m+1}}{2}}^{\frac{N_{m+1}}{2}-1} \tilde{H}_{z,m+1}^n (f_{mi,m+1}^n - g_{mi,m+1}^n) \\
& + 2\pi \eta_0 \sum_{n=-\frac{N_{m+1}}{2}}^{\frac{N_{m+1}}{2}-1} \tilde{E}_{t,m+1}^n h_{mi,m+1}^n \\
= & 0 \tag{19b}
\end{aligned}$$

where  $i = 0, \dots, N_m - 1$ . Note that when we compute Green's functions to construct the internal state equation, the dielectric parameters of the  $(m + 1)$ th material must be used.

#### D. Algebraic System Matrix Assembly

If we let the field point index  $i$  in (19) change from 0 to  $N_m - 1$ , (19) can be written as the compact matrix form

$$[\mathbf{Z}_{m-1} \quad \mathbf{Z}_m \quad \mathbf{Z}_{m+1}] \begin{bmatrix} \mathbf{I}_{m-1} \\ \mathbf{I}_m \\ \mathbf{I}_{m+1} \end{bmatrix} = \mathbf{V}_m \tag{20}$$

where  $\mathbf{Z}_m \in \mathbb{C}^{2N_m \times 2N_m}$ ,  $\mathbf{Z}_{m-1} \in \mathbb{C}^{2N_m \times 2N_{m-1}}$ ,  $\mathbf{Z}_{m+1} \in \mathbb{C}^{2N_m \times 2N_{m+1}}$ ,  $\mathbf{I}_m \in \mathbb{C}^{2N_m \times 1}$ ,  $\mathbf{I}_{m-1} \in \mathbb{C}^{2N_{m-1} \times 1}$ ,  $\mathbf{I}_{m+1} \in \mathbb{C}^{2N_{m+1} \times 1}$ , and  $\mathbf{V}_m \in \mathbb{C}^{2N_m \times 1}$ . The first  $N_m$  elements of  $\mathbf{I}_m$  are  $\tilde{H}_{zm}^n$  with  $n$  increasing from  $-(N_m/2)$  to  $(N_m/2) - 1$ , and its last  $N_m$  elements are  $\tilde{E}_{tm}^n$  with  $n$  increasing from  $-(N_m/2)$  to  $(N_m/2) - 1$ .  $\mathbf{I}_{m-1}$  and  $\mathbf{I}_{m+1}$  can be assembled in a similar way if we replace  $m$  with  $m - 1$  or  $m + 1$  in  $\mathbf{I}_m$ . In order to show the assembly of  $\mathbf{Z}_m$ , we first decompose it into

$$\mathbf{Z}_m = \begin{bmatrix} \mathbf{Z}_m^{11} & \mathbf{Z}_m^{12} \\ \mathbf{Z}_m^{21} & \mathbf{Z}_m^{22} \end{bmatrix} \tag{21}$$

where the dimensions of  $\mathbf{Z}_m^{11}$ ,  $\mathbf{Z}_m^{12}$ ,  $\mathbf{Z}_m^{21}$ , and  $\mathbf{Z}_m^{22}$  are all  $N_m \times N_m$ . The element in the  $i$ th row and  $n$ th column of  $\mathbf{Z}_m^{11}$  and  $\mathbf{Z}_m^{12}$  is, respectively,

$$\mathbf{Z}_m^{11}(i, n) = \frac{1}{2} \exp \left[ -j \left( n - 1 - \frac{N_m}{2} \right) \theta_{m,i-1} \right] \delta_{n,i}$$

$$\begin{aligned}
& -2\pi \left( f_{m(i-1),m}^{n-1-\frac{N_m}{2}} - g_{m(i-1),m}^{n-1-\frac{N_m}{2}} \right) \\
& + 4j \left( u_{m(i-1),m}^{n-1-\frac{N_m}{2}} - v_{m(i-1),m}^{n-1-\frac{N_m}{2}} \right) \tag{22a}
\end{aligned}$$

$$\mathbf{Z}_m^{12}(i, n) = \eta_0 \left( 2\pi h_{m(i-1),m}^{n-1-\frac{N_m}{2}} - 4j w_{m(i-1),m}^{n-1-\frac{N_m}{2}} \right) \tag{22b}$$

where  $\delta_{n,i}$  is the Kronecker symbol.  $\mathbf{Z}_m^{21}$  has the same expression as that of  $\mathbf{Z}_m^{11}$ , and  $\mathbf{Z}_m^{22}$  has the same expression as that of  $\mathbf{Z}_m^{12}$ . However, the dielectric parameters of the  $(m + 1)$ th material must be used when we evaluate Green's functions.  $\mathbf{Z}_{m-1}$  and  $\mathbf{Z}_{m+1}$  can be assembled in a similar way by referring to (19). However,  $\mathbf{Z}_{m-1}^{21}$ ,  $\mathbf{Z}_{m-1}^{22}$ ,  $\mathbf{Z}_{m+1}^{11}$ , and  $\mathbf{Z}_{m+1}^{12}$  are zeros. The first  $N_m$  elements of  $\mathbf{V}_m$  are  $H_{zm}^{\text{inc}}(\theta_{mi})$  with  $i$  increasing from 0 to  $N_m - 1$ . The last  $N_m$  elements are zero. Finally, we let  $m$  change from 1 to  $M$  and, respectively, cascade  $\mathbf{Z}_m$ ,  $\mathbf{I}_m$ , and  $\mathbf{V}_m$ , and obtain the whole matrix equation

$$\mathbf{ZI} = \mathbf{V} \tag{23}$$

where  $\mathbf{Z}$  is a complex matrix with the dimensions of  $2\sum_{m=1}^M N_m \times 2\sum_{m=1}^M N_m$ .  $\mathbf{I}$  and  $\mathbf{V}$  are complex vectors with the dimensions of  $2\sum_{m=1}^M N_m \times 1$ .  $\mathbf{Z}$  is a block-by-block tridiagonal matrix, since the total magnetic fields in the  $m$ th boundary are only contributed by equivalent current in the  $(m - 1)$ th,  $m$ th, and  $(m + 1)$ th boundaries. However, each block is a dense matrix. Equation (23) can be directly solved by an iterative method. Once  $\tilde{H}_z$  and  $\tilde{E}_t$  in all elliptical boundaries are obtained, they can be substituted into (8) to compute the corresponding spatial-domain field values. On the other hand, the scattered fields at the receiver array can be evaluated by first applying the discretized spectral-domain operators  $\tilde{\mathcal{K}}_{rq}^{h,s}$ ,  $\tilde{\mathcal{L}}_{rq}^{h,s}$ ,  $\tilde{\mathcal{K}}_{rq}^{ex,s}$ ,  $\tilde{\mathcal{K}}_{rq}^{ey,s}$ ,  $\tilde{\mathcal{L}}_{rq}^{ex,s}$ , and  $\tilde{\mathcal{L}}_{rq}^{ey,s}$  to  $\tilde{H}_z$  and  $\tilde{E}_t$  and then performing the inverse Fourier transform, such as (8).

### III. NUMERICAL RESULTS

In this section, we present two numerical examples to verify the expected exponential accuracy of the proposed SIM for EM scattering from multilayered nonconcentric elliptical cylinders by comparing its computation results with those from MoM as well as FEM, which is implemented through the commercial software COMSOL. Note that the FEM results are used as criteria in our work, since FEM can achieve reliable computation accuracy as long as the discretized mesh is small enough. It is assumed that the elliptical cylinders are immersed in a vacuum. The magnetic dipoles are used to excite TE<sub>z</sub> EM waves. The operating frequency is 300 MHz. All the simulations and numerical computations are performed on a workstation with a 48-core Intel Xeon 6248R 3.0G CPU and 1024-GB RAM. COMSOL automatically uses parallel computation. In the SIM, the Fourier transforms are realized by paralleled fast algorithms.

#### A. Three-Layer Isotropic Nonconcentric Elliptical Cylinders

As shown in Fig. 2, three isotropic elliptical cylinders are illuminated by TE<sub>z</sub>-polarized EM waves, which are simultaneously excited by three unit magnetic dipole transmitters. The geometry parameters of each elliptical boundary and the

TABLE I

GEOMETRY PARAMETERS OF EACH ELLIPSE AND THE ISOTROPIC DIELECTRIC PARAMETERS OF THE MEDIUM ON ITS INNER SIDE

Parameters	Ellipse #1	#2	#3
center coordinate	(-1.0, 0.0)	(-0.5, -1.5)	(0.2, -2.0)
horizontal half axis length	6.0	4.5	3.0
vertical half axis length	8.0	4.5	2.0
$\epsilon$	1.9	3.0	5.2
$\sigma$	1.0	2.0	3.0
$\mu$	1.5	2.0	0.9

Remark: the units of position and length are meters; the unit of  $\sigma$  is mS/m.

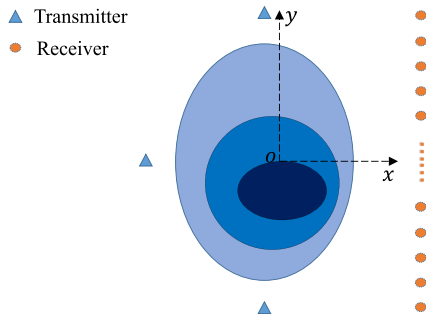


Fig. 2. Three nonconcentric elliptical magnetodielectric isotropic cylinders illuminated by  $TE_z$ -polarized EM waves, which are excited by three magnetic dipole transmitters.

isotropic dielectric parameters of the medium on its inner side are listed in Table I. Note that the ellipses are numbered from the outermost one to the innermost one. Three transmitters are located at  $(-9.0, 0.0)$ ,  $(-1.0, 10.0)$ , and  $(-1.0, -10.0)$  m, respectively. Totally, 49 receivers are evenly placed at a straight line in the  $\hat{y}$ -direction. The lowermost one is located at  $(9.0, -10.0)$  m, and the increment between the two receivers is 0.41666 m.

First, let us verify the computation accuracy of the tangential fields  $H_z$  and  $E_t$  along three elliptical boundaries. Here, we pick up 61 representative sampling points in three boundaries, and the corresponding EM field values are displayed in Fig. 3. The FEM results by COMSOL are used as a reference. As can be seen, SIM can achieve reliable accuracy even when the spatial sampling densities along the elliptical boundaries are lowered to 2.5 PPW. Unfortunately, the traditional MoM must increase the SD to 19.8 PPW in order to reach good matches with the FEM results. Precise calculations show that the relative errors of  $H_z$  for SIM with SD = 2.5 PPW, MoM with SD = 19.8 PPW, and MoM with SD = 2.5 PPW compared with FEM results are 0.19%, 0.34%, and 5.3%, respectively. Similarly, the relative errors of  $E_t$  for the aforementioned three situations are 0.06%, 0.37%, and 5.7%, respectively. These error data indicate that SIM only needs less than 3-PPW SD to achieve reliable computation accuracy. However, MoM needs to increase the SD to near 20 PPW in order to reach the same accuracy.

Then, let us verify the computation accuracy of scattered fields at the receiver array. We also compare the EM field values for SIM with SD = 2.5 PPW, MoM with SD = 19.8 PPW, and MoM with SD = 2.5 PPW. Fig. 4 shows the corresponding results. Numerical calculations show that

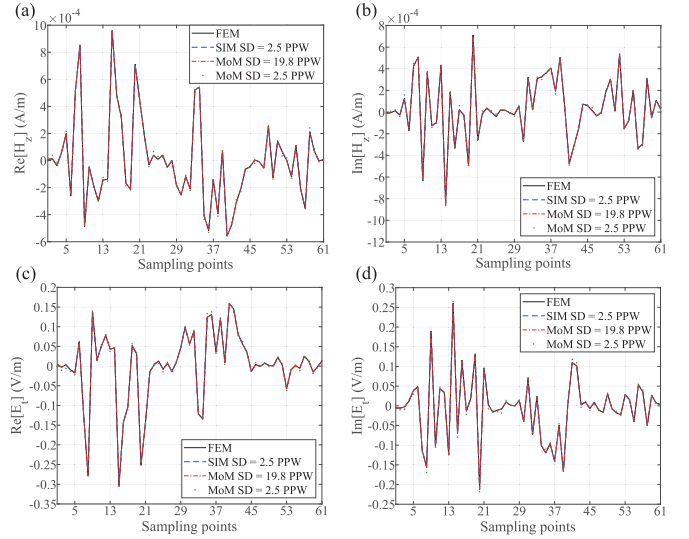


Fig. 3. Comparisons of the tangential EM fields along three elliptical boundaries computed by FEM, MoM, and SIM when the spatial SD takes different values. (a) Real part of  $H_z$ . (b) Imaginary part of  $H_z$ . (c) Real part of  $E_t$ . (d) Imaginary part of  $E_t$ .

the relative errors of  $E_x^{\text{sct}}$  for the three situations are 0.09%, 0.18%, and 3.0%, respectively, the relative errors of  $E_y^{\text{sct}}$  are 0.11%, 0.22%, and 3.5%, respectively, and the relative errors of  $H_z^{\text{sct}}$  are 0.10%, 0.22%, and 3.3%, respectively. It can be seen that the scattered fields at the receiver array computed by SIM can still achieve the 0.1% error when the SD is lowered to 2.5 PPW. However, the computation error of MoM is in the order of one hundredth for the same SD. In addition, COMSOL takes 178.3 s and consumes 59.8-GB memory to complete the computation. By contrast, SIM only takes 2.0 s and consumes 2.4-GB memory to compute the scattered fields when the SD = 2.5 PPW. When SD = 19.8 PPW, MoM takes 52.1 s and consumes 4.1-GB memory to reach the same computation accuracy. Clearly, SIM outperforms both FEM and MoM for computation efficiency.

Finally, let us check the exponential accuracy property of SIM when the spatial SD in the elliptical boundaries gradually increases. Fig. 5(a)-(c) shows the variations of relative errors of the scattered fields at the receiver array when SD increases from 1.27 to 24.8 PPW. For SIM, when SD is less than 5.0, the error decreases exponentially. However, when SD is larger than 5.0, the error almost remains unchanged with the order of  $10^{-13}$ . This means that the 5.0 PPW SD for the spectral-domain integral method is saturated when the multilayered elliptical cylinders are isotropic. Another possible reason for this nearly constant error is the numerical calculation errors of both SIM and FEM. They are numerical solvers instead of analytical ones. As a result, the relative error between them cannot decrease to infinitesimal. Compared with SIM, the errors of MoM decay rather slow as SD increases. Even when we increase its value to near 25 PPW, the relative errors of the scattered fields are in the order of 0.1%. Clearly, MoM can never reach the same accuracy as SIM, since the sampling points in the elliptical boundaries are independent if the integral equation is solved in the spatial domain. Fig. 5(d)

TABLE II  
GEOMETRY PARAMETERS OF EACH ELLIPSE AND THE ANISOTROPIC DIELECTRIC PARAMETERS OF THE MEDIUM ON ITS INNER SIDE

Parameters	Ellipse		#1	#2	#3	#4	#5	#6	#7	#8	#9	#10
	center coordinate		(-1.1, -1.1)	(-1.0, -0.9)	(-1.1, -1.0)	(-0.9, -0.4)	(-1.3, -0.5)	(-1.0, 0.3)	(-1.2, -1.2)	(-1.4, -1.5)	(-1.8, -1.2)	(-3.0, -1.0)
horizontal half axis length		17.0	14.0	12.0	9.0	8.0	7.0	6.0	4.0	3.0	2.0	1.0
vertical half axis length		14.0	12.5	12.0	10.0	9.0	7.0	4.0	3.0	2.0	1.0	
$\varepsilon_x$		1.5	2.0	2.5	3.0	3.5	4.0	4.5	5.0	5.5	6.0	
$\varepsilon_y$		1.4	1.8	2.2	2.6	3.0	3.4	3.8	4.2	4.6	5.0	
$\sigma_x$		0.1	0.2	0.3	0.4	0.5	0.6	0.7	0.8	0.9	1.0	
$\sigma_y$		0.2	0.1	0.3	0.5	0.4	0.5	0.2	0.3	0.4	0.5	
$\mu$		1.1	1.2	1.3	1.4	1.5	1.6	1.7	1.8	1.9	2.0	

Remark: the units of position and length are meters; the unit of  $\sigma$  is mS/m.

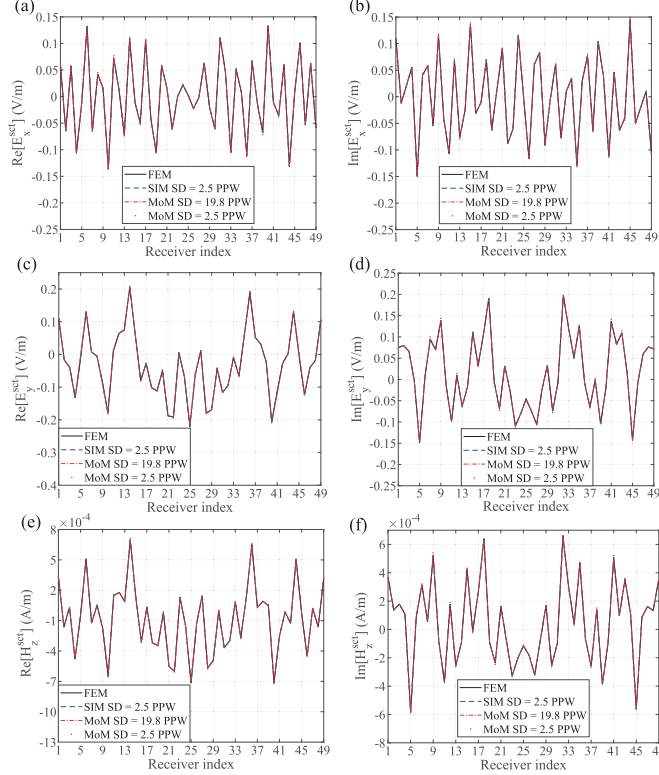


Fig. 4. Comparisons of the scattered EM fields at the receiver array computed by FEM, MoM, and SIM when the spatial sampling densities along the elliptical boundaries take different values. (a) Real part of  $E_x^{\text{scat}}$ . (b) Imaginary part of  $E_x^{\text{scat}}$ . (c) Real part of  $E_y^{\text{scat}}$ . (d) Imaginary part of  $E_y^{\text{scat}}$ . (e) Real part of  $H_z^{\text{scat}}$ . (f) Imaginary part of  $H_z^{\text{scat}}$ .

shows the CPU time and the number of unknowns in the discretized integral equations versus the mean error of the scattered fields of three components when SD increases from 1.27 to 24.8 PPW. It is obvious that the error of SIM is much lower than that of MoM for the same CPU time or the number of unknowns. In other words, MoM will consume much more computation resources than SIM if we try to use both of them to reach the same accuracy.

### B. Ten-Layer Electrically Large Biaxially Anisotropic Nonconcentric Elliptical Cylinders

In this case, we increase the layer number and also use the biaxially anisotropic medium for the cylinders, which raises the complexity of the spatial medium distribution. Meanwhile, the size of the scatterer is also increased. The purpose of these changes is to test the adaptability and verify

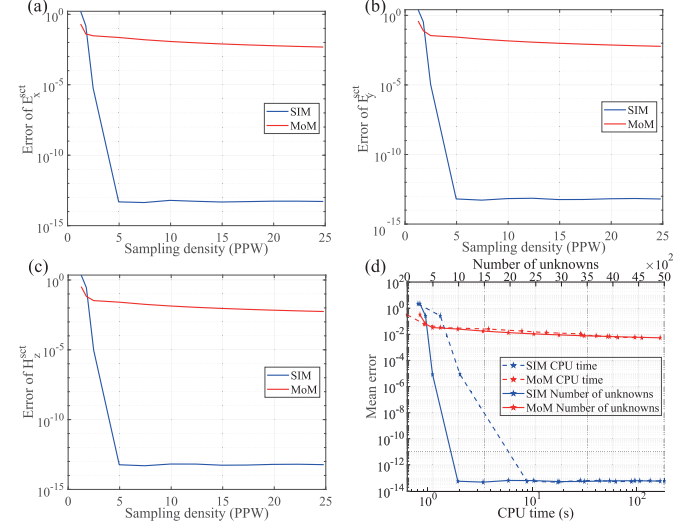


Fig. 5. Comparisons of the computation error variations of scattered fields with SD, CPU time, and the number of unknowns in the integral equations for SIM and MoM. (a) Error of  $E_x^{\text{scat}}$  changes with SD. (b) Error of  $E_y^{\text{scat}}$  changes with SD. (c) Error of  $H_z^{\text{scat}}$  changes with SD. (d) Mean error versus CPU time and the number of unknowns.

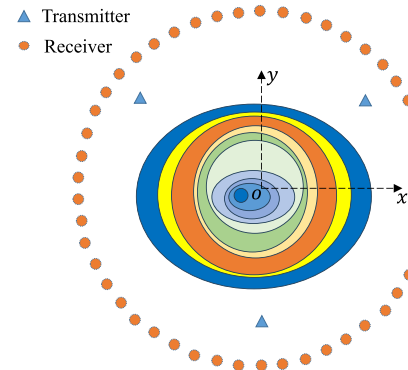


Fig. 6. Ten nonconcentric elliptical magnetodielectric anisotropic cylinders illuminated by TE<sub>z</sub>-polarized EM waves, which are excited by three magnetic dipoles transmitters.

the superiority of the proposed SIM. As shown in Fig. 6, ten anisotropic nonconcentric elliptical cylinders are illuminated by the TE<sub>z</sub>-polarized EM waves, which are excited by three unit magnetic dipoles located at (15.8, 11.0), (-18.6, 11.0), and (-0.6, -18.8) m, respectively. The specific parameters of ten elliptical cylinders are listed in Table II. Note that the outermost ellipse has a perimeter of nearly 100.0 m, which is about 100 times the wavelength in the background medium.

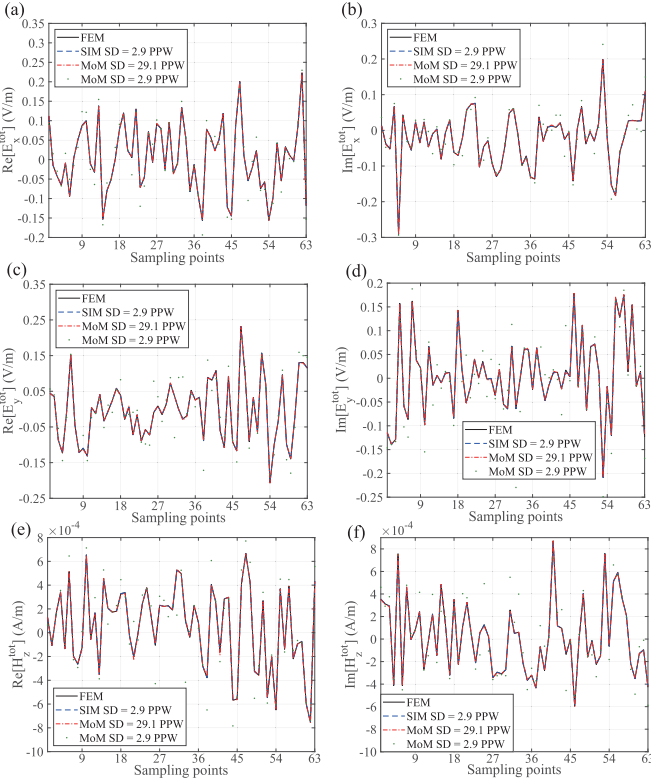


Fig. 7. Comparisons of the total EM fields at 63 typical sampling points inside the computational domain computed by FEM, MoM, and SIM when the spatial sampling densities along the elliptical boundaries take different values. (a) Real part of  $E_x^{\text{tot}}$ . (b) Imaginary part of  $E_x^{\text{tot}}$ . (c) Real part of  $E_y^{\text{tot}}$ . (d) Imaginary part of  $E_y^{\text{tot}}$ . (e) Real part of  $H_z^{\text{tot}}$ . (f) Imaginary part of  $H_z^{\text{tot}}$ .

Totally, 49 receivers are evenly placed on a circle whose center is located at  $(1.1, -1.4)$  m, and the radius is 24.0 m.

Now, let us verify the computation accuracy of the total fields  $E_x^{\text{tot}}$ ,  $E_y^{\text{tot}}$ , and  $H_z^{\text{tot}}$  at  $7 \times 9$  sampling points inside the computational domain. The sampling point located at the bottom left corner has the coordinate  $(-21.2, -16.0)$  m. The increment between two sampling points in either the  $\hat{x}$ -direction or the  $\hat{y}$ -direction is 5.0 m. Fig. 7 shows the comparisons of the total EM fields at 63 sampling points computed by FEM, SIM, and MoM. It is obvious that SIM still can achieve good matches with FEM when the SD is lower than 3.0 PPW. However, MoM must increase the SD to ten times larger in order to reach reliable matches. Precise calculations show that the relative errors of  $E_x^{\text{tot}}$  for SIM with SD = 2.9 PPW, MoM with SD = 29.1 PPW, and MoM with SD = 2.9 PPW compared with FEM results are 0.09%, 1.5%, and 28%, respectively, the errors of  $E_y^{\text{tot}}$  for these three situations are 0.07%, 1.8%, and 45%, respectively, and the errors of  $H_z^{\text{tot}}$  for these three situations are 0.10%, 1.8%, and 40%, respectively. By comparing these error data with those for the isotropic case discussed in Section III-A, we can see that SIM still can achieve similar computation accuracy even for electrically large anisotropic elliptical scatterers when the SD is low. Unfortunately, the computation of MoM is not reliable if the SD is lowered to near 3.0 PPW. Even when it is increased to near 30.0 PPW, MoM can only achieve around one hundredth computation error. These discrepancies are further validated by the computation of the scattered fields

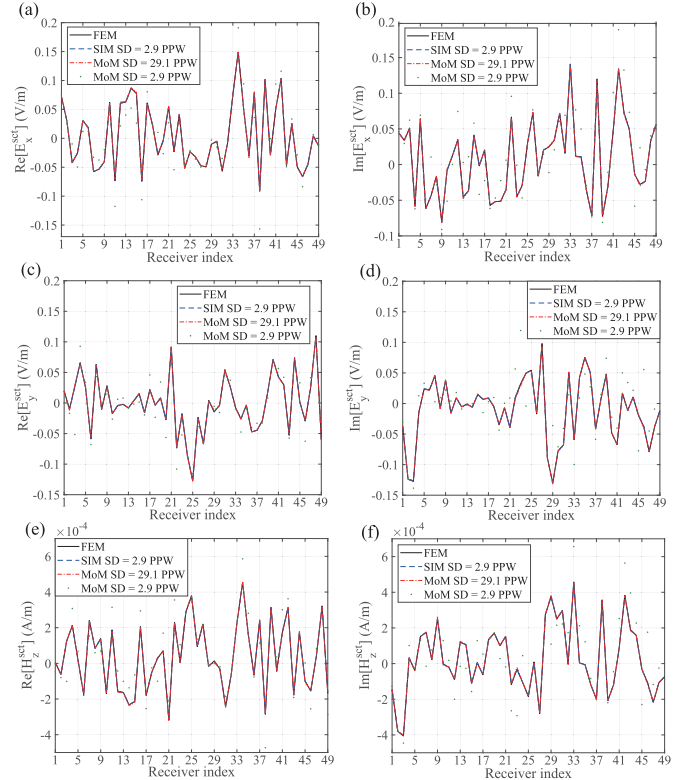


Fig. 8. Comparisons of the scattered EM fields at the receiver array computed by FEM, MoM, and SIM when the spatial sampling densities along the elliptical boundaries take different values. (a) Real part of  $E_x^{\text{scat}}$ . (b) Imaginary part of  $E_x^{\text{scat}}$ . (c) Real part of  $E_y^{\text{scat}}$ . (d) Imaginary part of  $E_y^{\text{scat}}$ . (e) Real part of  $H_z^{\text{scat}}$ . (f) Imaginary part of  $H_z^{\text{scat}}$ .

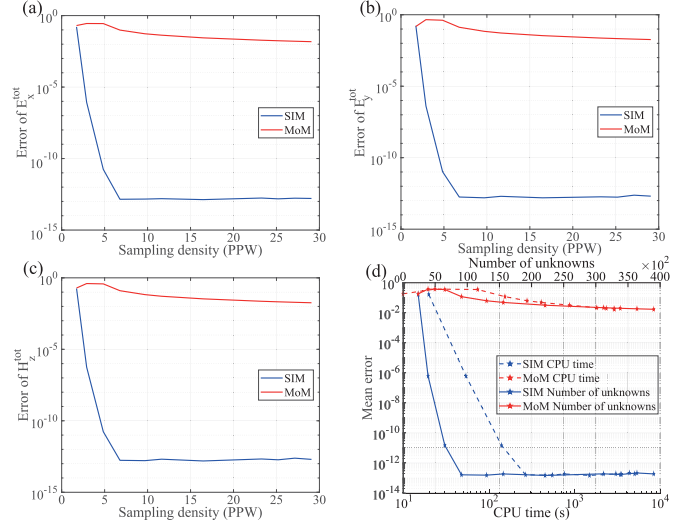


Fig. 9. Comparisons of the computation error variations of total fields at 63 typical sampling points with SD, CPU time, and the number of unknowns in the integral equations for SIM and MoM. (a) Error of  $E_x^{\text{tot}}$  changes with SD. (b) Error of  $E_y^{\text{tot}}$  changes with SD. (c) Error of  $H_z^{\text{tot}}$  changes with SD. (d) Mean error versus CPU time and the number of unknowns.

at the receiver array, which are shown in Fig. 8. The relative errors of the scattered fields are in the order of one thousandth, several tens percent, and one hundredth for SIM with SD = 2.9 PPW, MoM with SD = 29.1 PPW, and MoM with SD = 2.9 PPW, respectively. In addition, for this electrically large anisotropic case, COMSOL takes 788 s and consumes 245-GB

memory to complete the computation. MoM takes 2918 s and consumes 186-GB memory for the SD of 29.1 PPW. However, SIM only takes 53 s and consumes 4.5-GB memory to achieve reliable computation accuracy.

Fig. 9(a)–(c) shows the variations of relative errors of the total EM fields at the 63 sampling points for different SD values. We can see that SIM still has exponential accuracy for electrically large anisotropic elliptical cylindrical scatterers. However, compared with the error variations shown in Fig. 5(a)–(c) for isotropic scatterers, the errors of both SIM and MoM decay slower for anisotropic scatterers. Such a difference may be caused by the complexity of the spatial medium distribution. Fig. 9(d) shows the CPU time and the number of unknowns versus the mean error of the total fields. The variations of errors have similar trends as those shown in Fig. 5(d). However, SIM outperforms MoM more prominently in both time and accuracy for this anisotropic case compared with the previous isotropic case.

#### IV. CONCLUSION AND DISCUSSION

In this work, we developed the SIM for EM scattering from multilayered nonconcentric elliptical magnetodielectric cylinders illuminated by TE<sub>z</sub>-polarized waves. The dielectric materials filling each cylinder can either be isotropic or biaxially anisotropic. Both the unknown tangential EM fields along the multiple elliptical boundaries and the 2-D Green's functions are expanded by the Fourier series. A subtraction method is adopted to smoothen the strong singularity of Green's functions caused by the proximity of the source point and the field point in the elliptical boundary. This guarantees Green's functions can be correctly expanded by the Fourier series with low orders. Consequently, the whole discretized integral equation is solved in the spectral domain with a limited number of Fourier coefficients.

Two numerical examples are used to show the superiority of the proposed SIM to the traditional MoM. It is found that SIM can achieve reliable computation accuracy, i.e., the error is in the order of one thousandth, as long as the spatial SD is higher than 3.0 PPW. By contrast, the traditional MoM needs at least 20.0 PPW to reach the same computation accuracy for isotropic scatterers. When the multilayered elliptical cylinders become anisotropic and their electrical sizes are huge, MoM can only lower the computation error to the order of one hundredth even if we increase the SD to 30.0 PPW. SIM is able to maintain computation accuracy with low computational cost for both simple and complex elliptical magnetodielectric cylinders.

Finally, we want to emphasize three points here. First, both the formula derivation and numerical examples are given for smooth elliptical boundaries in this work. However, the proposed SIM can be directly applied to any homogeneous scatterers having smooth boundaries as long as the EM fields and Green's functions in the boundaries can be expanded by Fourier series with low orders. Second, we use the magnetic dipoles as transmitters in the numerical examples for the convenience of verification via FEM. SIM is also applicable to the scenario with plane wave excitation. Third, the proposed

SIM can also be directly applied to a smooth metallization boundary as long as we discard  $\mathbf{M}$  in (2).

#### APPENDIX A

It is assumed both the EM fields and the background medium are invariant along the  $\hat{z}$ -direction in the 2-D problem. As a result, we have  $\nabla = \hat{x}(\partial/\partial x) + \hat{y}(\partial/\partial y)$ . In the unbounded homogeneous isotropic background medium with the complex relative permittivity  $\epsilon_b$  and the relative permeability  $\mu_b$ , the 2-D source point locates at  $\rho' = \hat{x}x' + \hat{y}y'$ , while the 2-D field point locates at  $\rho = \hat{x}x + \hat{y}y$ . For the TE<sub>z</sub> mode, we have  $\mathbf{E} = \hat{x}E_x + \hat{y}E_y$ ,  $\mathbf{H} = \hat{z}H_z$ ,  $\mathbf{J} = \hat{x}J_x + \hat{y}J_y$ , and  $\mathbf{M} = \hat{z}M_z$ . The 2-D scalar Green's function is written as follows:

$$g(\rho, \rho') = -\frac{j}{4} H_0^{(2)}(k_b \rho) \quad (\text{A1})$$

where  $H_0^{(2)}$  is the zeroth-order Hankel function of the second kind,  $k_b = k_0(\epsilon_b \mu_b)^{1/2}$  is the wavenumber of the background medium, and  $\rho = |\rho - \rho'|$  is the distance between the field point and the source point. We then define the auxiliary magnetic vector potential  $\mathbf{A} = \mu_b \mu_0 [g \hat{x} \hat{x} + g \hat{y} \hat{y}] \cdot \mathbf{J}$  and the auxiliary electric vector potential  $\mathbf{F} = \epsilon_b \epsilon_0 [g \hat{z} \hat{z}] \cdot \mathbf{M}$ . The EM fields are related to them by [39]

$$\mathbf{E} = -j\omega \mathbf{A} - j \frac{1}{\omega \mu_0 \epsilon_0 \mu_b \epsilon_b} \nabla(\nabla \cdot \mathbf{A}) - \frac{1}{\epsilon_0 \epsilon_b} \nabla \times \mathbf{F} \quad (\text{A2a})$$

$$\mathbf{H} = \frac{1}{\mu_0 \mu_b} \nabla \times \mathbf{A} - j\omega \mathbf{F} - j \frac{1}{\omega \mu_0 \epsilon_0 \mu_b \epsilon_b} \nabla(\nabla \cdot \mathbf{F}). \quad (\text{A2b})$$

By substituting  $g$  in (A1) in to (A2), we obtain the final 2-D dyadic Green's function components for an isotropic medium

$$\begin{aligned} G_{EJ}^{xx} &= -\frac{\omega \mu_b \mu_0}{4} H_0^{(2)}(k_b \rho) \\ &\quad + \frac{k_b}{4\omega \epsilon_0 \epsilon_b \rho} H_1^{(2)}(k_b \rho) - \frac{k_b^2}{4\omega \epsilon_0 \epsilon_b} H_2^{(2)}(k_b \rho) \cos^2 \phi \end{aligned} \quad (\text{A3a})$$

$$G_{EJ}^{yx} = -\frac{k_b^2}{8\omega \epsilon_0 \epsilon_b} H_2^{(2)}(k_b \rho) \sin 2\phi \quad (\text{A3b})$$

$$G_{EJ}^{xy} = G_{EJ}^{yx} \quad (\text{A3c})$$

$$\begin{aligned} G_{EJ}^{yy} &= -\frac{\omega \mu_b \mu_0}{4} H_0^{(2)}(k_b \rho) \\ &\quad + \frac{k_b}{4\omega \epsilon_0 \epsilon_b \rho} H_1^{(2)}(k_b \rho) - \frac{k_b^2}{4\omega \epsilon_0 \epsilon_b} H_2^{(2)}(k_b \rho) \sin^2 \phi \end{aligned} \quad (\text{A3d})$$

$$G_{HJ}^{zx} = G_{EM}^{xz} = -\frac{j k_b}{4} H_1^{(2)}(k_b \rho) \sin \phi \quad (\text{A3e})$$

$$G_{HJ}^{zy} = G_{EM}^{yz} = \frac{j k_b}{4} H_1^{(2)}(k_b \rho) \cos \phi \quad (\text{A3f})$$

$$G_{HM}^{zz} = -\frac{\omega \epsilon_0 \epsilon_b}{4} H_0^{(2)}(k_b \rho) \quad (\text{A3g})$$

where  $\phi$  is the angle between the vector  $\rho - \rho'$  and the  $\hat{x}$ -axis with  $\cos \phi = ((x - x')/\rho)$  and  $\sin \phi = ((y - y')/\rho)$ . In addition, the 2-D dyadic Green's functions for the TM<sub>z</sub> mode can be directly evaluated based on (A3) according to the duality theorem.

## APPENDIX B

For the  $\text{TE}_z$  mode, it is assumed that the unbounded homogeneous biaxially anisotropic background medium has the complex relative permittivity  $\bar{\epsilon}_b = \hat{x}\hat{x}\epsilon_{xb} + \hat{y}\hat{y}\epsilon_{yb}$  and the relative permeability  $\mu_b$ . By taking the similar method given in [40, Sec. V], we construct the auxiliary magnetic vector potential  $\mathbf{A}$  and the auxiliary electric vector potential  $\mathbf{F}$  as follows:

$$\mathbf{A} = \hat{x} \left[ -\frac{j\mu_b\mu_0}{4} \sqrt{\frac{\epsilon_{yb}}{\epsilon_{xb}}} H_0^{(2)}(k_{xb}\rho_x) \right] J_x + \hat{y} \left[ -\frac{j\mu_b\mu_0}{4} \sqrt{\frac{\epsilon_{xb}}{\epsilon_{yb}}} H_0^{(2)}(k_{yb}\rho_y) \right] J_y \quad (\text{B1a})$$

$$\mathbf{F} = \hat{z} \left[ -\frac{j\epsilon_0\sqrt{\epsilon_{xb}\epsilon_{yb}}}{4} H_0^{(2)}(k_{xb}\rho_x) \right] M_z \quad (\text{B1b})$$

where  $k_{xb} = k_0(\mu_b\epsilon_{xb})^{1/2}$ ,  $\rho_x = ([(\epsilon_{yb}/\epsilon_{xb})(x-x')^2 + (y-y')^2])^{1/2}$ ,  $k_{yb} = k_0(\mu_b\epsilon_{yb})^{1/2}$ ,  $\rho_y = ([(\epsilon_{yb}/\epsilon_{xb})(y-y')^2 + (x-x')^2])^{1/2}$ , and  $k_{xb}\rho_x = k_{yb}\rho_y = k_0(\mu_b)^{1/2}([(\epsilon_{yb}(x-x')^2 + \epsilon_{xb}(y-y')^2])^{1/2}$ . Different from (A2), in a 2-D biaxially anisotropic medium, the EM fields are related to the vector potentials by

$$\mathbf{E} = -j\omega\mathbf{A} - j\frac{1}{\omega\mu_0\epsilon_0\mu_b\epsilon_{xb}\epsilon_{yb}} \nabla(\nabla \cdot \bar{\epsilon}_b \mathbf{A}) - \frac{\bar{\epsilon}_b^{-1}}{\epsilon_0} \nabla \times \mathbf{F} \quad (\text{B2a})$$

$$\mathbf{H} = \frac{1}{\mu_0\mu_b} \nabla \times \mathbf{A} - j\omega\mathbf{F} - j\frac{\bar{\epsilon}_b^{-1}}{\omega\mu_0\epsilon_0\mu_b} \nabla(\nabla \cdot \mathbf{F}) \quad (\text{B2b})$$

where  $\epsilon_{xb}\epsilon_{yb}$  in the denominator is the gauge for an anisotropic medium suggested by Chew [41]. By substituting (B1) into (B2), we obtain the final 2-D dyadic Green's function components for a biaxially anisotropic medium

$$G_{EJ}^{xx} = -\frac{\omega\mu_b\mu_0}{4} \left( \frac{\epsilon_{yb}}{\epsilon_{xb}} \right)^{\frac{1}{2}} H_0^{(2)}(k_{xb}\rho_x) + \frac{k_{xb}}{4\omega\epsilon_0\epsilon_{yb}\rho_x} \left( \frac{\epsilon_{yb}}{\epsilon_{xb}} \right)^{\frac{3}{2}} H_1^{(2)}(k_{xb}\rho_x) - \frac{k_{xb}^2}{4\omega\epsilon_0\epsilon_{yb}} \left( \frac{\epsilon_{yb}}{\epsilon_{xb}} \right)^{\frac{5}{2}} H_2^{(2)}(k_{xb}\rho_x) \cos^2 \phi_x \quad (\text{B3a})$$

$$G_{EJ}^{vx} = -\frac{k_{xb}^2}{8\omega\epsilon_0\epsilon_{yb}} \left( \frac{\epsilon_{yb}}{\epsilon_{xb}} \right)^{\frac{3}{2}} H_2^{(2)}(k_{xb}\rho_x) \sin 2\phi_x \quad (\text{B3b})$$

$$G_{EJ}^{xy} = -\frac{k_{yb}^2}{8\omega\epsilon_0\epsilon_{xb}} \left( \frac{\epsilon_{xb}}{\epsilon_{yb}} \right)^{\frac{3}{2}} H_2^{(2)}(k_{yb}\rho_y) \sin 2\phi_y \quad (\text{B3c})$$

$$G_{EJ}^{yy} = -\frac{\omega\mu_b\mu_0}{4} \left( \frac{\epsilon_{xb}}{\epsilon_{yb}} \right)^{\frac{1}{2}} H_0^{(2)}(k_{yb}\rho_y) + \frac{k_{yb}}{4\omega\epsilon_0\epsilon_{xb}\rho_y} \left( \frac{\epsilon_{xb}}{\epsilon_{yb}} \right)^{\frac{3}{2}} H_1^{(2)}(k_{yb}\rho_y) - \frac{k_{yb}^2}{4\omega\epsilon_0\epsilon_{xb}} \left( \frac{\epsilon_{xb}}{\epsilon_{yb}} \right)^{\frac{5}{2}} H_2^{(2)}(k_{yb}\rho_y) \sin^2 \phi_y \quad (\text{B3d})$$

$$G_{HJ}^{zx} = G_{EM}^{xz} = -\frac{jk_{xb}}{4} \left( \frac{\epsilon_{yb}}{\epsilon_{xb}} \right)^{\frac{1}{2}} H_1^{(2)}(k_{xb}\rho_x) \sin \phi_x \quad (\text{B3e})$$

$$G_{HJ}^{zy} = G_{EM}^{yz} = \frac{jk_{yb}}{4} \left( \frac{\epsilon_{xb}}{\epsilon_{yb}} \right)^{\frac{1}{2}} H_1^{(2)}(k_{yb}\rho_y) \cos \phi_y \quad (\text{B3f})$$

$$G_{HM}^{zz} = -\frac{\omega\epsilon_0\sqrt{\epsilon_{xb}\epsilon_{yb}}}{4} H_0^{(2)}(k_{xb}\rho_x) \quad (\text{B3g})$$

where  $\cos \phi_x = ((x-x')/\rho_x)$ ,  $\cos \phi_y = ((y-y')/\rho_y)$ ,  $\sin \phi_x = ((y-y')/\rho_x)$ , and  $\sin \phi_y = ((x-x')/\rho_y)$ . The  $\text{TM}_z$  mode 2-D dyadic Green's functions for a biaxially anisotropic medium can also be evaluated based on (B3) according to the duality theorem.

## REFERENCES

- [1] M. Zhou, L. Ying, L. Lu, L. Shi, J. Zi, and Z. Yu, "Electromagnetic scattering laws in Weyl systems," *Nature Commun.*, vol. 8, p. 1388, Aug. 2017.
- [2] A. V. Ryzhkov and D. S. Zrnic, *Radar Polarimetry for Weather Observations*. Gewerbestrasse, Switzerland: Springer Nature, 2019, ch. 1.
- [3] J.-M. Jin, *The Finite Element Method in Electromagnetics*. Hoboken, NJ, USA: Wiley, 2014.
- [4] G. C. Cohen, *Higher-Order Numerical Methods for Transient Wave Equations*. Berlin, Germany: Springer-Verlag, 2001.
- [5] S. D. Gedney, *Introduction to the Finite-Difference Time-Domain (FDTD) Method for Electromagnetics*. Cham, Switzerland: Springer Nature, 2011.
- [6] R. F. Harrington, *Field Computation by Moment Methods*. New York, NY, USA: Wiley-IEEE Press, 1993.
- [7] X. Han et al., "3D finite-element forward modeling of airborne EM systems in frequency-domain using octree meshes," *IEEE Trans. Geosci. Remote Sens.*, vol. 60, 2022, Art. no. 5912813.
- [8] P. Kosmas and C. M. Rappaport, "Time reversal with the FDTD method for microwave breast cancer detection," *IEEE Trans. Microw. Theory Techn.*, vol. 53, no. 7, pp. 2317–2323, Jul. 2005.
- [9] X. Millard and Q. H. Liu, "Simulation of near-surface detection of objects in layered media by the BCGS-FFT method," *IEEE Trans. Geosci. Remote Sens.*, vol. 42, no. 2, pp. 327–334, Feb. 2004.
- [10] J. Wang, J. Liu, M. Zhuang, and Q. H. Liu, "Spectral-element spectral-integral method for EM scattering by doubly periodic objects in fully anisotropic layered media," *IEEE Trans. Microw. Theory Techn.*, early access, Apr. 27, 2023, doi: 10.1109/TMTT.2023.3263398.
- [11] B. R. Spies, "Electrical and electromagnetic borehole measurements: A review," *Surveys Geophysics*, vol. 17, no. 4, pp. 517–556, Jul. 1996.
- [12] W. Cai, U. K. Chettiar, A. V. Kildishev, and V. M. Shalaev, "Optical cloaking with metamaterials," *Nature Photon.*, vol. 1, no. 4, pp. 224–227, Apr. 2007.
- [13] B. Dang et al., "A uniform linear multi-coil array-based borehole transient electromagnetic system for non-destructive evaluations of downhole casings," *Sensors*, vol. 18, no. 8, p. 2707, Aug. 2018.
- [14] C. Liu et al., "Synthesized magnetic field focusing for the non-destructive testing of oil and gas well casing pipes using pulsed eddy-current array," *IEEE Trans. Magn.*, vol. 58, no. 9, pp. 1–10, Sep. 2022.
- [15] M. Thiel and A. Dreher, "Dyadic Green's function of multilayer cylindrical closed and sector-structures for waveguide, microstrip-antenna, and network analysis," *IEEE Trans. Microw. Theory Techn.*, vol. 50, no. 11, pp. 2576–2579, Nov. 2002.
- [16] Z. Zhang, S. Yang, Y. Chen, S. Qu, and J. Hu, "Fast analysis of parallel-plate cylindrical Luneberg lens antennas through dyadic Green's functions," *IEEE Trans. Microw. Theory Techn.*, vol. 66, no. 10, pp. 4327–4337, Oct. 2018.
- [17] H. Wang, P. So, S. Yang, W. J. R. Hoefer, and H. Du, "Numerical modeling of multicomponent induction well-logging tools in the cylindrically stratified anisotropic media," *IEEE Trans. Geosci. Remote Sens.*, vol. 46, no. 4, pp. 1134–1147, Apr. 2008.
- [18] M. Dehmollaian, N. Chamanara, and C. Caloz, "Wave scattering by a cylindrical metasurface cavity of arbitrary cross section: Theory and applications," *IEEE Trans. Antennas Propag.*, vol. 67, no. 6, pp. 4059–4072, Jun. 2019.
- [19] B. Ivisic, Z. Sipus, and S. Hrabar, "Analysis of uniaxial multilayer cylinders used for invisible cloak realization," *IEEE Trans. Antennas Propag.*, vol. 57, no. 5, pp. 1521–1527, May 2009.
- [20] A. Mirzaei, A. E. Miroshnichenko, I. V. Shadrivov, and Y. S. Kivshar, "All-dielectric multilayer cylindrical structures for invisibility cloaking," *Sci. Rep.*, vol. 5, no. 1, p. 9574, Apr. 2015.
- [21] H. A. Ragheb, L. Shafai, and M. Hamid, "Plane wave scattering by a conducting elliptic cylinder coated by a nonconfocal dielectric," *IEEE Trans. Antennas Propag.*, vol. 39, no. 2, pp. 218–223, Feb. 1991.

- [22] G. P. Zouros, "Oblique electromagnetic scattering from lossless or lossy composite elliptical dielectric cylinders," *J. Opt. Soc. Amer. A, Opt. Image Sci.*, vol. 30, no. 2, pp. 196–205, Feb. 2013.
- [23] A. Soltani, Z. Rahmani, and E. Heidari-Semiromi, "Electromagnetic waves scattering from an infinite elliptical metal cylinder covered by a plasma layer in presence of external magnetic field," *Optik*, vol. 243, Oct. 2021, Art. no. 166846.
- [24] Z. Xiang and Y. Lu, "Electromagnetic dyadic Green's function in cylindrically multilayered media," *IEEE Trans. Microw. Theory Techn.*, vol. 44, no. 4, pp. 614–621, Apr. 1996.
- [25] C. Tokgoz and G. Dural, "Closed-form Green's functions for cylindrically stratified media," *IEEE Trans. Microw. Theory Techn.*, vol. 48, no. 1, pp. 40–49, Jan. 2000.
- [26] Z. Xiang and D. Shen, "A hybrid BEM/WTM/DFT technique for analysis of the EM scattering from open-ended circular cavities with cylindrically periodic terminations," *IEEE Trans. Antennas Propag.*, vol. 52, no. 9, pp. 2479–2485, Sep. 2004.
- [27] H. Moon, F. L. Teixeira, and B. Donderici, "Stable pseudoanalytical computation of electromagnetic fields from arbitrarily-oriented dipoles in cylindrically stratified media," *J. Comput. Phys.*, vol. 273, pp. 118–142, Sep. 2014.
- [28] K. E. Warnick and W. Cho Chew, "Accuracy of the method of moments for scattering by a cylinder," *IEEE Trans. Microw. Theory Techn.*, vol. 48, no. 10, pp. 1652–1660, Oct. 2000.
- [29] A. C. Cangellaris and R. Lee, "Finite element analysis of electromagnetic scattering from inhomogeneous cylinders at oblique incidence," *IEEE Trans. Antennas Propag.*, vol. 39, no. 5, pp. 645–650, May 1991.
- [30] Z. Gong and A. W. Glisson, "A hybrid equation approach for the solution of electromagnetic scattering problems involving two-dimensional inhomogeneous dielectric cylinders," *IEEE Trans. Antennas Propag.*, vol. 38, no. 1, pp. 60–68, Jan. 1990.
- [31] N. N. Bojarski, "Scattering by a cylinder: A fast exact numerical solution," *J. Acoust. Soc. Amer.*, vol. 75, no. 2, pp. 320–323, Feb. 1984.
- [32] G. T. Schuster, "A fast exact numerical solution for the acoustic response of concentric cylinders with penetrable interfaces," *J. Acoust. Soc. Amer.*, vol. 87, no. 2, pp. 495–520, 1990.
- [33] F. Q. Hu, "A spectral boundary integral equation method for the 2D Helmholtz equation," *J. Comput. Phys.*, vol. 120, no. 2, pp. 340–347, Sep. 1995.
- [34] J. Liu and Q. H. Liu, "A spectral integral method (SIM) for periodic and nonperiodic structures," *IEEE Microw. Wireless Compon. Lett.*, vol. 14, no. 3, pp. 97–99, Mar. 2004.
- [35] E. Şimşek, J. Liu, and Q. H. Liu, "A spectral integral method (SIM) for layered media," *IEEE Trans. Antennas Propag.*, vol. 54, no. 6, pp. 1742–1749, Jun. 2006.
- [36] Y.-K. Li, J. Hu, W.-F. Huang, Z.-P. Nie, and Q. H. Liu, "A spectral integral method for smooth multilayered bodies of revolution," *IEEE Trans. Antennas Propag.*, vol. 65, no. 8, pp. 4146–4154, Aug. 2017.
- [37] Z. Guan, Y. Zhang, F. Han, C. Zhu, and Q. H. Liu, "Fast exponentially convergent solution of electromagnetic scattering from multilayer concentric magnetodielectric cylinders by the spectral integral method," *IEEE Trans. Microw. Theory Techn.*, vol. 68, no. 6, pp. 2183–2193, Jun. 2020.
- [38] L. Tsang, J. A. Kong, K.-H. Ding, and C. O. Ao, *Scattering of Electromagnetic Waves: Numerical Simulations*. New York, NY, USA: Wiley, 2001, ch. 4.
- [39] C. A. Balanis, *Advanced Engineering Electromagnetics*. New York, NY, USA: Wiley, 2012, ch. 6.
- [40] K. A. Michalski and J. R. Mosig, "Multilayered media Green's functions in integral equation formulations," *IEEE Trans. Antennas Propag.*, vol. 45, no. 3, pp. 508–519, Mar. 1997.
- [41] W. C. Chew, "Vector potential electromagnetics with generalized Gauge for inhomogeneous media: Formulation," *Prog. Electromagn. Res.*, vol. 149, pp. 69–84, 2014.



**Zhen Guan** received the Ph.D. degree in computational science from the School of Mathematical Sciences and the Institute of Electromagnetics and Acoustics, Xiamen University, Xiamen, China, in 2022.

From March 2021 to April 2022, she was a Joint-Training Ph.D. Student with the Mathematical Institute of the Department of Mathematics and Computer Science, Free University Berlin, Berlin, Germany. Since July 2022, she has been with Tianjin University of Technology, Tianjin, China, where she is currently a Lecturer at the School of Science. Her research interests include the fast algorithms for computational electromagnetics and electromagnetic scattering and inverse scattering problems and their applications in engineering.



**Jiawen Li** received the B.S. degree in electronic science and technology from the Wuhan University of Technology of China, Wuhan, China, in 2011, and the Ph.D. degree in electromagnetic field and microwave technology from Xiamen University, Xiamen, China, in 2023.

Since August 2023, he has been with Guangxi Normal University, Guangxi, China, where he is currently an Assistant Professor with the School of Electronic and Information Engineering. His research interests include electromagnetic scattering in complex media and the full-wave inversion of anisotropic targets.



**Feng Han** (Senior Member, IEEE) received the B.S. degree in electronic science from Beijing Normal University, Beijing, China, in 2003, the M.S. degree in geophysics from Peking University, Beijing, in 2006, and the Ph.D. degree in electrical engineering from Duke University, Durham, NC, USA, in 2011.

From 2011 to 2015, he was a Software Engineer at Wavenovation Inc., Xiamen, China. In July 2015, he joined the Institute of Electromagnetics and Acoustics, Xiamen University, Xiamen, China, as an Assistant Professor, where he was promoted to an Associate Professor in 2020. In October 2023, he joined the School of Computing and Information Technology, Great Bay University, Guangdong, China, as an Associate Professor. He has published over 50 articles in refereed journals. His research interests include electromagnetic scattering and inverse scattering in complex media, multiparametric and multidimensional hybrid electromagnetic full-wave inversion, fast electromagnetic full-wave inversion based on machine learning, configuration of the antenna array for electromagnetic inverse problems, and geophysical electromagnetic exploration and inversion.